

# Spintronic Sensors

*Spintronic sensors start from a variety of fundamental physical principles: anisotropic magnetoresistance, giant magnetoresistance, and tunneling magnetoresistance, and have a wide variety of device geometries, sensitivities, intrinsic noise mechanisms, biasing, and interconnection schemes, depending on the specific application. Applications span from industrial applications to biosensor and biomedical applications.*

By PAULO P. FREITAS, Senior Member IEEE, RICARDO FERREIRA, AND SUSANA CARDOSO, Member IEEE

**ABSTRACT** | This paper describes how magnetoresistive materials can be optimized and integrated in magnetic field sensor devices. Giant magnetoresistive (GMR) and tunnel magnetoresistive (TMR) can provide advantageous solutions for a wide range of applications, of which some are described here. Considerations on field sensitivities, intrinsic noise mechanisms, biasing, and integration schemes are presented.

**KEYWORDS** | Biochips; magnetic detectivities; magnetoresistive sensors; microelectrodes; noise

## I. INTRODUCTION

Spintronic sensors based on the magnetoresistive (MR) effect have been widely explored over the past years for many applications, strongly inspired by the success of the magnetic recording technology. These devices directly convert the magnetic field into a voltage or resistance with a dc bias current supply. As the MR sensors can be fabricated with high yields in 200 mm diameter substrates and also integrated on CMOS wafers already including the readout electronics, the MR technology

can be made very compact and versatile. Designing a high-performance MR sensor [either spin valves (SV) or magnetic tunnel junctions (MTJ)] requires strategies for improving the magnetic field detection level while reducing the noise. Reducing the sensor area increases the resolution for fields that change over small distances. MR sensors are thereby suitable for array applications due to their relative small size and low power requirements when compared to coils or fluxgates and low-field sensing techniques, such as SQUIDs. MR sensors operate with two orders of magnitude less power and almost three orders of magnitude lower cost than the competing technologies. Moreover, since low magnetostriction alloys are used in the free sensing layers, incorporation on flexible substrates is also possible, therefore opening a realm of applications in which MR can offer advantages.

Some figures of merit are the small dimensions (micrometric range), reduced cost, and high magnetic field sensitivity at room temperature. MR sensors can be optimized to detect fields ranging from few tens mT down to tens pT, therefore spanning 8–9 orders of magnitude in the magnetic field range. Highly sensitive magnetometers have been developed based on spin-exchange relaxation mechanisms [1], but the outstanding performance for fT fields detection costs space and simplicity, as the device requires optics and laser accessories. Other devices based on quantum wires [2] could offer competitive detection limits ( $80 \text{ fT}/\text{Hz}^{0.5}$ ); however, fabrication methods are not yet in line with top down, CMOS compatible, technological approaches. The recent advances on magneto-electric materials combined with strategies for enhanced noise rejection could offer interesting solutions for pT detection [3].

This paper focuses on magnetoresistive sensors only, because large bandwidth devices can operate from DC

Manuscript received January 7, 2016; revised April 29, 2016; accepted May 27, 2016. Date of publication September 12, 2016; date of current version September 16, 2016. INESC-MN acknowledges FCT funding through the IN Associated Laboratory through Pest-OE/CTM/LA0024/2011. INL acknowledges partial funding from ON2 project from PO Norte. This work was supported in part by projects PEST-OE/EEI/LA0021/2011, EXCL/CTM-NAN/0441/2012, PTDC/EEI-PRO/3219/2012, IMAGIC EU-FP7-288381, and MAGNETRODES EU-FP7-ICT-600730.

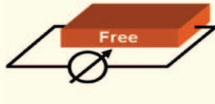
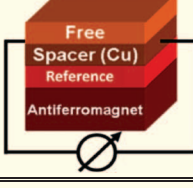
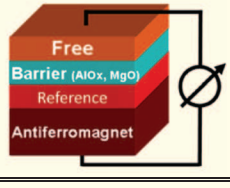
**P. P. Freitas** and **R. Ferreira** are with INL—International Iberian Nanotechnology Laboratory, Braga, 4715-330 Portugal (e-mail: paulo.freitas@inl.int; ricardo.ferreira@inl.int).

**S. Cardoso** is with the Physics Department, Instituto Superior Técnico (IST), Universidade de Lisboa, Lisboa, 1000 Portugal, and also with INESC-Microsystems and Nanotechnologies (INESC-MN), 1000-029 Lisboa, Portugal (e-mail: scardoso@inesc-mn.pt).

Digital Object Identifier: 10.1109/JPROC.2016.2578303

0018-9219 © 2016 IEEE. Personal use is permitted, but republication/redistribution requires IEEE permission.  
See [http://www.ieee.org/publications\\_standards/publications/rights/index.html](http://www.ieee.org/publications_standards/publications/rights/index.html) for more information.

**Table 1** Typical Key Properties of Magneto Resistive Sensors

	AMR	GMR- Spinvalves	TMR- Magnetic Tunnel Junctions (MTJ)
<i>Physical principle</i>	Anisotropic MR	Giant MR	Spin dependent tunneling
<i>Thin film structure</i>	Simple Buffer/free/cap	Multilayers, several material compositions Buffer/free/spacer/reference/pinning/cap	Complex multilayers, several material compositions Buffer/free/barrier/reference/pinning/cap
<i>Magnetoresistance (MR) [%]<sup>#</sup></i>	2-6	6-20	50% ( $Al_2O_3$ amorphous barrier) 300% ( $MgO$ crystalline barrier)
<i>Sensor linear range [mT]<sup>&amp;</sup></i>	0.1-10	1-5	2-10
<i>Thermal treatment [°C]<sup>\$</sup></i>	Not required	Typically 220-280°C	Typically 280-340°C
<i>Reference layer</i>	No, needs external	Yes (interface exchange biased through an antiferromagnetic film)	Yes (interface exchange biased through an antiferromagnetic film)
<i>Electrical robustness against electrostatic discharge</i>	Excellent	Excellent	Good
<i>General geometry and readout scheme</i>			

<sup>s</sup> Temperature for a post-deposition/processing annealing under a magnetic field.

<sup>&</sup> Typical values obtained from the sensor transfer curve (R vs B), for sensor dimensions ranging few micrometers.

<sup>#</sup> These values are registered from literature, where optimized linear MR sensor responses were reported. Notice that higher values can be achieved (e.g., 600% for  $MgO$  devices [14]) but not in a sensor configuration.

to the GHz range, with an adjustable impedance (from  $1\ \Omega$  to  $100\ k\Omega$ ) and magnetic sensitivity range (from  $0.1\ mT$  to  $100\ mT$ ), which can be matched to specific application requirements. Moreover, the spatial resolution scales with the sensor dimensions (down to tens nm), making them attractive for applications in which a small footprint, good field sensitivity, and good spatial resolution need to be addressed simultaneously.

This paper presents a comprehensive description of the materials optimization wherein the relevant parameters for a successful integration in functional devices are described. The range of applications is vast, spanning from industrial applications (integrated magnetic compass, angle and linear sensors [4], current sensors [5], scanners and magnetic imagers, including non-destructive testing) to biosensor and biomedical applications (DNA and protein biochips [6], integrated cell cytometers, imaging systems-MCG and magnetic resonance, and microelectrodes for neuronal magnetic field probing [7]). Sensor layout and full system integration is described and exemplified for some of these applications.

## II. MATERIALS AND SENSOR DESIGN

### A. Magnetoresistive Materials

A MR sensor is based on magnetoresistive thin film materials deposited on wafers or flat substrates and then patterned into the required shape and size, using top-down lithography techniques. There are some materials (e.g., Co, NiFe, CoFe, and their alloys) exhibiting a magnetoresistive effect at room temperature [8].

When defined into a controlled shape and accessed with two electrical contacts, their resistance is a function of the magnetic orientation with respect to the current direction, so a magnetoresistive ratio  $MR = (R_{high} - R_{low})/R_{low}$  (i.e., giving a percentage change of the resistance), can be determined. Since the experimental verification of this effect in 1986 [9], engineered multilayer stacks with controlled thickness (typically 1 nm thick films, with accuracy better than 0.1 nm), have been explored for tailored properties of the devices. The control of film thickness, composition, interfaces, crystalline structure, homogeneity and reproducibility for large scale production are possible only through the technological advances in thin film deposition and lithography methods.

As a result, several generations of MR sensors have been developed and successfully validated in commercial products. Although having different physical principles of operation, MR sensors are historically classified according to the MR ratio as briefly summarized in Table 1. Anisotropic MR (AMR), giant MR (GMR), and tunnel MR (TMR) sensors are presently very mature technologies, optimized from simple thin film materials (AMR) toward high-performance devices (TMR). Figures of merit (some of them listed in Table 1) are the MR ratio, thermal stability, and the ability to obtain a linear resistance versus field characteristic, with controlled linear range. The latter is described in next section.

Improved stability against external magnetic fields and thermal effects are desired specifications for a field sensor, and have been independently, resulting in engineered multilayer stacks called spin-valve (SV) [10]. Here, the thin

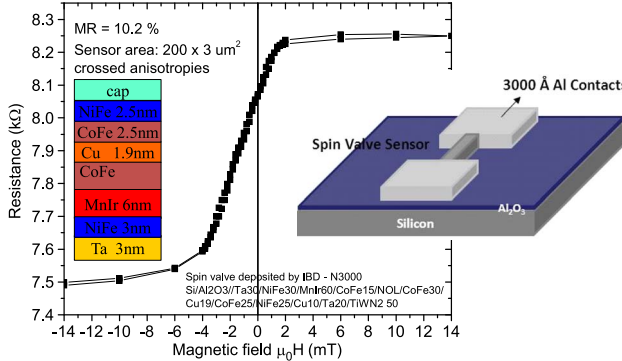


**Fig. 1.** Spin valve sensor transfer curve and geometry. The SV film materials and thicknesses are represented, where the two ferromagnetic layers are separated by a nonmagnetic film (1.9 nm thick copper film).

film structure comprises: 1) a reference layer (pinned through exchange biasing with an adjacent antiferromagnetic film, AF, such as MnIr or MnPt [11]) which is stable under the influence of very large external magnetic fields ( $\sim 40$  mT) and temperature (over  $250$  °C), 2) a magnetic-free layer that aligns to the magnetic field to be measured, and 3) a spacer that decouples the free and reference magnetic layers. The basic layer structure of such a system and an example of a sensor patterned into a sensing element, having a linear transfer curve ( $R$  vs.  $H$ ), are shown in Fig. 1.

Increasing demands from the industry motivated the use of additional layers for enhanced magnetic rigidity of the reference layer. These strategies are well described in [12]. In TMR sensors, the magnetic film structure is similar to the one optimized for the SV sensor, varying mainly in the spacer between the free and reference layers: here, the metallic spacer is replaced by a thin insulating spacer layer (e.g., Al<sub>2</sub>O<sub>3</sub> or MgO, 1 nm thick) that forms a tunnel barrier [13]. In this case, the devices are also called magnetic tunnel junctions (MTJ). For the current to pass across the barrier, these devices need to be patterned into current-perpendicular-to-plane (CPP) devices, when compared with the other MR sensors, which are generally current in plane (CIP) (see Table 1). Although being a continuous insulator, when a bias voltage is applied across the barrier, a finite current flows through the junction because of quantum-mechanical tunneling [14]. TMR ratio values up to 70% [15] and 600% [16] have been reported, respectively, for Al<sub>2</sub>O<sub>3</sub> and MgO barriers that are combined with ferromagnetic electrodes based on CoFe/CoFeB films. Proper linearization usually requires a compromise between maximum signal and linear response characteristics; therefore, sensors have usually lower MR ratios (see Table 1) than those reported for test devices [17]. One example of a linearized sensor curve measured for Al<sub>2</sub>O<sub>3</sub>-based TMR device is presented in Fig. 2. The quality of the barrier growth conditions and the interface roughness have a

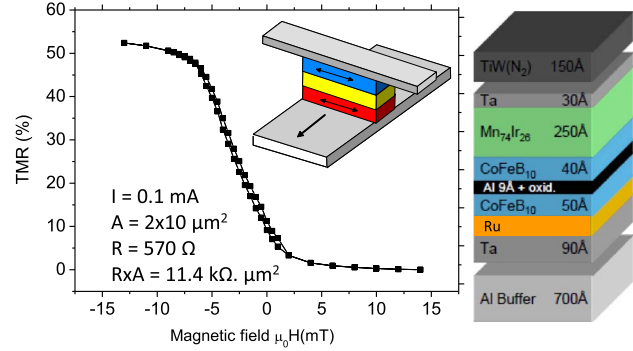


**Fig. 2.** Transfer curve measured for a perpendicular to plane magnetic tunnel junction based on amorphous AlOx barriers.

strong impact on the MR sensor properties. It is remarkable that Al<sub>2</sub>O<sub>3</sub> layers as thin as 0.6 nm can indeed be integrated into functional devices and perform as a tunnel barriers. Fig. 3 presents an example [18] where the impact of the barrier thickness on the MR levels and resistance-area product was investigated. Degradation of the MR signals observed for the thinner barriers is associated with the onset for the discontinuity of the Al film itself, with the consequences of promoting a competition between tunneling and resistive transport across the barrier. This phenomena was studied by several authors not only for Al<sub>2</sub>O<sub>3</sub> amorphous barriers (prepared by oxidation of ultrathin Al films) but also for MgO ultrathin crystalline films.

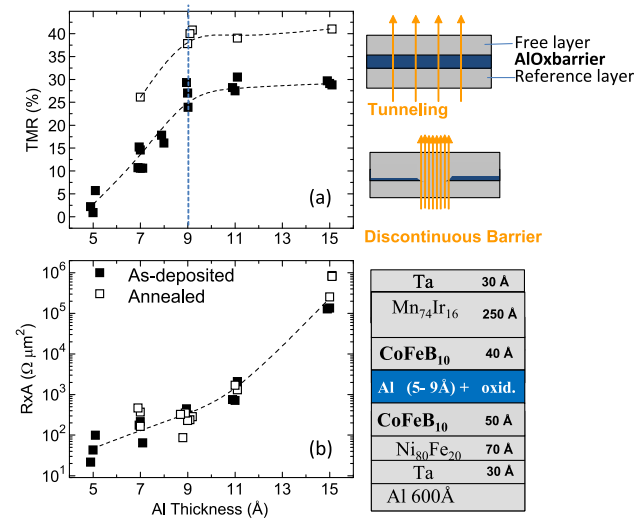


**Fig. 3.** (a) Magnetoresistance, TMR, and (b) resistance-area, Rx $A$  dependency on the tunnel barrier thickness, for AlOx-based structures deposited by ion beam oxidation of thin Al films. For ultrathin AlOx films (< 0.9 nm thick Al), the imperfections at the interfaces, grain boundaries, and pin-holes cause the reduction of the TMR signal as the tunnel electrical transport mechanism is replaced by the ohmic transport.

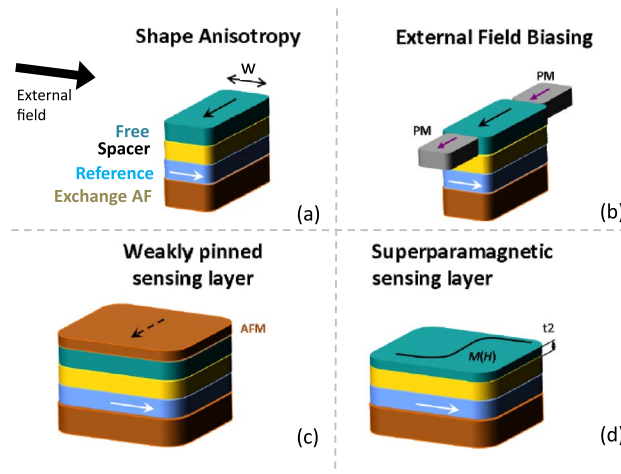


**Fig. 4.** Integrated linearization strategies commonly used for MR sensors. Adapted from [18]. The original publication is available at [www.epjap.org](http://www.epjap.org) (DOI: <http://dx.doi.org/10.1051/epjap/2015150214>).

## B. Strategies for Sensor Linearization

The use of MR sensors relies on the ability to integrate such thin film structures in a functional device with controlled output response under external magnetic fields. This corresponds to a situation when the reference and the free layers are orthogonal ( $90^\circ$ ) [19]. The sensor output can be calculated by taking into account all sources of magnetic field at the free layer: the external field ( $H$ ), the field created by the current density  $J$  ( $H_J$ ), anisotropy field ( $H_k$ ), demagnetizing field ( $H_{\text{dem}}$ ) and ferromagnetic coupling fields ( $H_f$ ). The effective anisotropy field is  $H_{\text{keff}} = H_k + H_{\text{dem}}$ . Therefore, spin valve and TMR sensor outputs in the linear regime are given by (1a) and (1b), respectively

$$\Delta V_{\text{SV}} = \text{MR} \cdot \frac{R_{\text{sq}} I}{2h} w \cdot \frac{H + H_J + H_f}{H_{\text{keff}}} \quad (1a)$$

$$\Delta V_{\text{TMR}} = \text{MR} \cdot \frac{R \cdot A \cdot I}{2wL} \cdot \frac{H + H_J + J_f}{H_{\text{keff}}} \quad (1b)$$

where  $R_{\text{sq}}$  is defined as  $\rho/t$  (where  $\rho$  is the SV resistivity). Also, the quantity  $R \cdot A$  (resistance—area product) shown in (1b) is constant for each barrier thickness.  $\text{MR}$  is the maximum magnetoresistance ratio,  $I$  is the biasing current, while  $w$  and  $L$  are geometrical dimensions (width and length).

Several strategies can be used to promote a linear response, free of hysteresis [20], as summarized in Fig. 4. One is to make use of the internal demagnetizing field through shape anisotropy [Fig. 4(a)], and reduce the size and aspect ratio of the sensor (this is effectively achieved

by reducing the sensor height  $h$ , therefore fulfilling the linearization condition:  $H_{\text{dem}} > H_k$  [21]).

Another strategy is to integrate on-chip an integrated permanent magnet (PM) to set a magnetic field [22] to stabilize the magnetization of the free layer along the length [see Fig. 4(b)]. Several applications (e.g., read heads for magnetic recording) rely on thin CoCrPt thin film elements patterned with the sensor element micro-fabrication process. Although effective for small sensors (length below  $\sim 10 \mu\text{m}$ ), this solution adds complexity and cost, and reduces the sensor sensitivity [23].

Linearization can also be accomplished through a third strategy [see Fig. 4(c)], consisting on adding an exchange biasing layer located near the free layer. Upon optimized annealing, it is possible to set the free layer with a weak pinning field, orthogonal to the reference layer [24], [25]. This strategy has been used specially for MgO-based MTJ sensors [26], where the demagnetizing fields created by the low magnetization ferromagnetic films (CoFeB) are not enough to promote a linear response, and the transfer curves are square or with some coercivity. Fig. 5 illustrates the impact of successive magnetic annealing steps carried out under crossed magnetic fields. The selected temperature for each annealing step is strongly dependent on the pinning layer (AF) thickness and composition. More details can be found in [26].

As a fourth strategy [see Fig. 4(d)], several authors have considered the reduction of the free layer thickness, toward a regime in which the magnetization is no longer in the plane of the film [27], [28]. Here, the material behaves intrinsically in the superparamagnetic regime, and linear responses are always achieved with very high sensitivities ( $\sim 35\%/\text{mT}$ ) [29], independent of the sensor dimensions. This could represent a major breakthrough for applications, provided that the drawbacks are surpassed. These are: a) the challenging control of the CoFeB thickness (with an accuracy below 0.01 nm) over large areas; b) the reduced MR values obtained for such thin films (MR below 80%, when compared with those obtained with 3 nm thick free layers (see Fig. 6); and c) the higher noise levels [30] obtained for these devices.

## C. Impact of Thin Film Homogeneity on Sensor Performance

Typically, AMR devices are relatively bulky due to the combination with flux concentrators and linearization elements that require mounting, assembly, and calibration, thus increasing the overall system cost. Therefore, the costs for a higher integration level (ASIC CMOS) would highly profit from the benefits of GMR and TMR technologies, which are less economic but incorporate a reference layer. These also require large volume production to be cost efficient; therefore, discrete electronics is a low cost option in many cases.

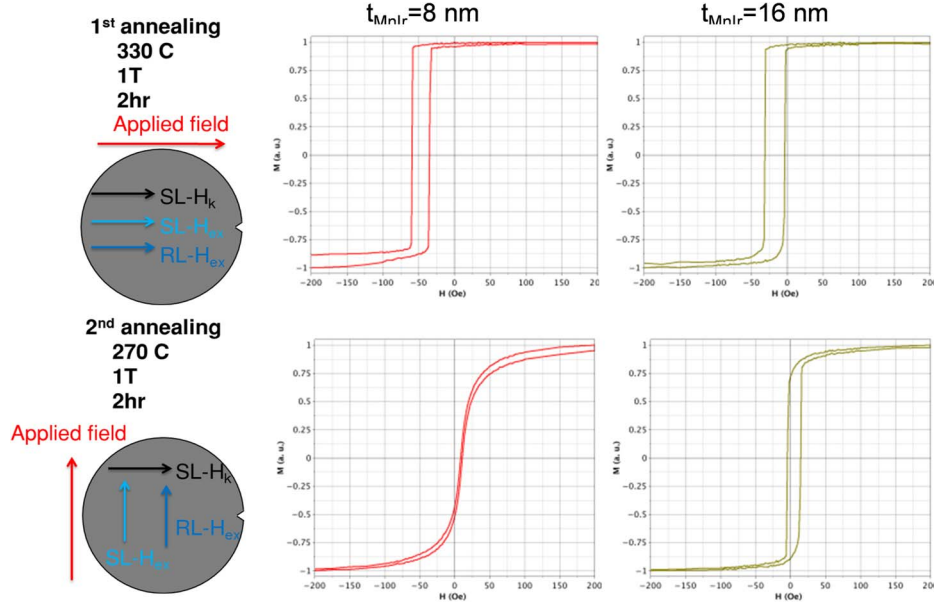


**Fig. 5.** Magnetic characteristics of a TMR stack incorporating a weak-pinned free layer for linearization assessment upon consecutive, crossed, magnetic anneals [structure: deposited in a Timaris tool with the stack 5 Ta/15 Ru/5 Ta/15 Ru/5 Ta/5 Ru/17 PtMn/2.0 CoFe/0.85 Ru/2.6 CoFeB<sub>20</sub>/MgO 1/3.0 CoFeB/0.21 Ta/8 NiFe/t<sub>MnIr</sub>/2 Ru/5 Ta/10 Ru (thickness in nm)].

The yield is very important during the processing of large area wafers. Sensors are being produced in 150 mm diameter wafers and already scale to 200 mm line integration. This requires an excellent control of film growth, material properties, and microfabrication processing over these large areas. For example, resistance and MR values dispersion over the wafers need to be monitored during batch processing. An example of a 150 mm wafer monitoring over the 18 chips distributed along the diagonal is shown in Fig. 7. Here,

the test sensors ( $2.5 \times 50 \mu\text{m}^2$ , spin valve sensors [35]) were measured after the metallization step to assess for homogeneity in the wafer area. MR levels are homogeneous (less than 0.5% deviations across wafer), while some dispersion is visible in the resistance, mainly due to the lithography process. Film was deposited by Ion beam (Nordiko3000 tool), with a uniformity of 1% over a 150 mm diameter area.

The uniformity of MTJ sensors is considerably more difficult to ensure across large substrates, especially in those that concern sensor applications. A typical example is shown in Figs. 8 and 9. The TMR and Rx A were extracted upon patterning and annealing in linear sensors made from the stack: [5 Ta/25 CuN]<sub>xc</sub>/5 Ta/5 Ru/20 IrMn/2 CoFe<sub>30</sub>/0.85 Ru/2.6 CoFe<sub>40</sub>B<sub>20</sub>/MgO/2 CoFe<sub>40</sub>B<sub>20</sub>/0.21 Ta/4 NiFe/0.20 Ru/6 IrMn/2 Ru/5 Ta/10 Ru [thicknesses in nm].

This is due to a distinctive property of TMR sensors: the exponential decrease of the tunneling current with the thickness of the tunnel barrier [13], as can be observed in the experimental results shown in Fig. 3(b). From a device perspective, this is interesting since the resistance of a TMR can be varied over many orders of magnitude simply by varying the thickness of the insulating spacer layer [35]. For a CPP device, the resistance depends on the area,  $A = \text{width} \times \text{length}$ . Therefore, the control parameter is the resistance-area product, Rx A, which should be a constant for each MTJ stack. A consequence is that sensors with the same dimensions can have tunable resistances by changing the barrier thickness and therefore not compromising its spatial resolution. This is not true for

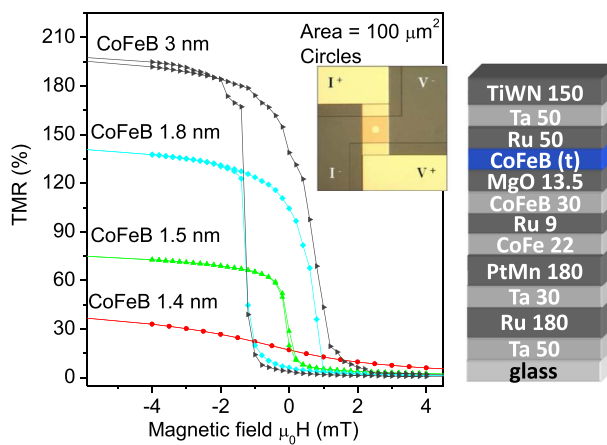


**Fig. 6.** Transfer curves for magnetic tunnel junction devices incorporating CoFeB free layers with varied thicknesses, denoting the onset of the ferromagnetic regime around 3 nm (corresponding to the maximum TMR signal).

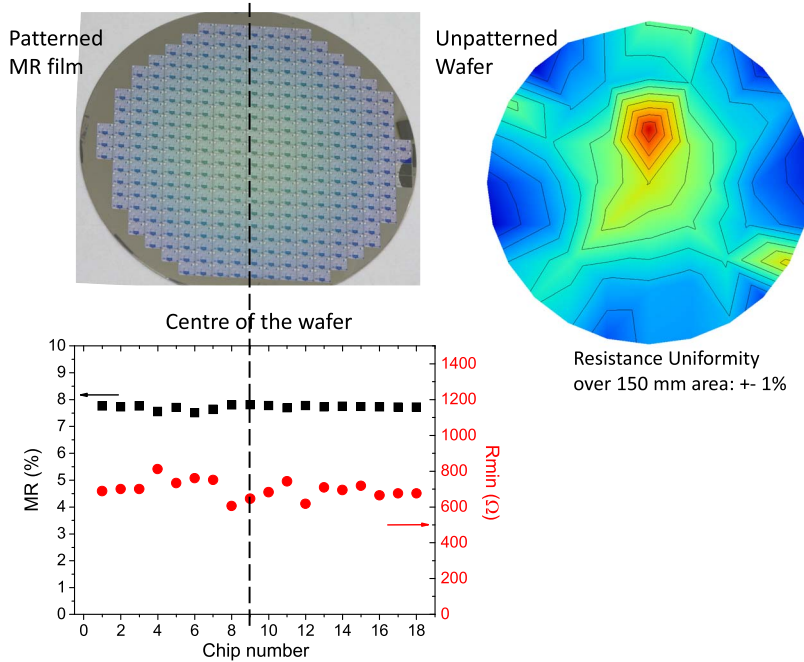


**Fig. 7.** Uniformity of spin valve sensors upon microfabrication across a 140 mm diameter region over the 150 mm substrate.

AMR and GMR sensors whereby the resistance increase is accomplished by the increase of the area.

The price to pay for this competitive advantage of the MTJ sensors is a much tighter demand for deposition uniformity. This can be easily understood by considering the data in Fig. 10.

Due to the exponential dependence on the MgO thickness, an RxA uniformity of 6.7% in the low RxA range (below  $10 \text{ } \Omega \mu\text{m}^2$ ) requires a variation of the MgO thickness smaller than 1% across a 200 mm wafer. This is a daunting feat considering that the thickness of the MgO in this RxA region is already smaller than 1 nm. However, the same uniformity in the MgO deposition will ensure

only a 13.2% RxA uniformity in the  $20 \text{ } \text{k}\Omega \mu\text{m}^2$ . If the MgO uniformity is decreased to 1.5%, the RxA uniformity in the  $20 \text{ } \text{k}\Omega \mu\text{m}^2$  range will degrade to 19.7%. Since the large resistance is one of the main advantages of MTJ sensors with respect to spin valves, this is a huge problem. Sensors with large resistances (meaning large output power and low power consumption) require large RxA values. And a given RxA non-uniformity threshold in the large RxA range always requires a much tighter control in the MgO deposition than in the low RxA region. In this sense, the requirements for the deposition of MTJ-based sensors are tighter than the requirements for the production of MRAM.

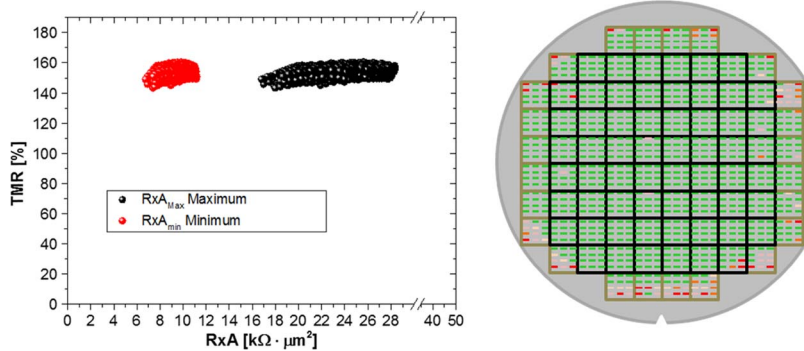


**Fig. 8.** (Left) TMR and RxA for a set of about 3500 MTJ sensors across a 200 mm diameter wafer measured in transport upon microfabrication and annealing. (Right) Wafer map with all working sensors marked in green and nonworking sensors (shorted or with open contacts) marked in red/orange. Most nonworking devices are caused by edge effects during the ion milling steps.

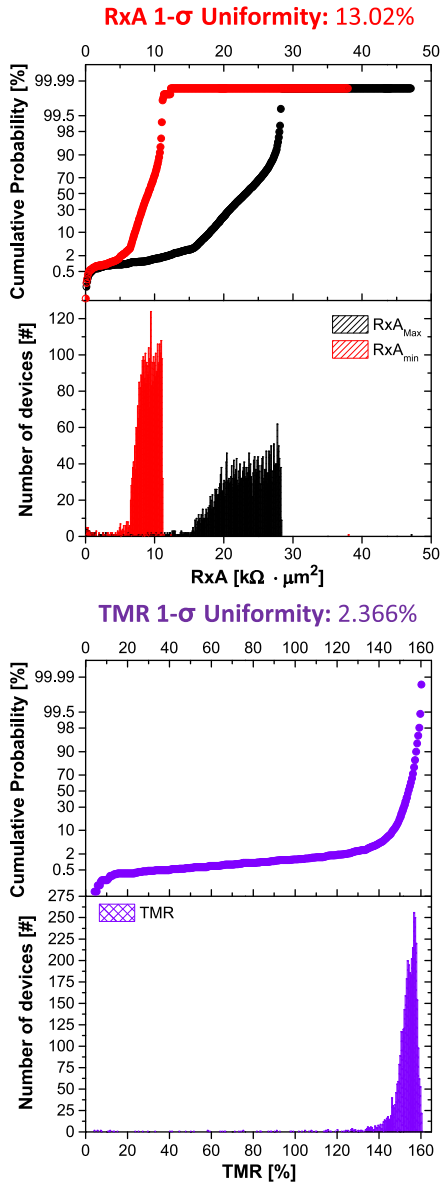


**Fig. 9.** (Top) Rx A cumulative distribution and histogram for the parallel and antiparallel states. (Bottom) TMR cumulative distribution and histogram.

### III. WHEATSTONE BRIDGE ARCHITECTURES: METHODS FOR REVERSING THE PINNED LAYER

One of the main challenges faced by MR sensors integrated in industrial applications concerns the requirement of immunity to thermal drifts. These sensors are often integrated in harsh environments in which temperature drifts of tenths of degrees cannot affect the magnetic field readout. As any other resistive sensor, the resistance of magnetic tunnel junctions and spin valves depends on temperature, and any output voltage fluctuation caused by temperature drifts must be distinguished from those caused by magnetic fields. The solution to

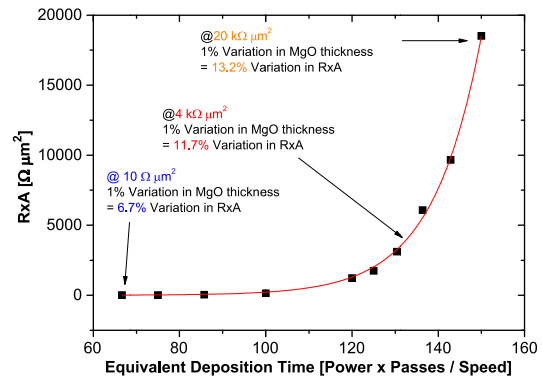


**Fig. 10.** Dependence of the Rx A (measured by CIPT) on the equivalent deposition time obtained in MTJs deposited in a dynamic deposition system. That is, the wafer is not static; therefore, the deposition time is determined by the number of passes below the magnetron divided by the stage speed.

this issue is the use of a Wheatstone Bridge architecture, as shown in Fig. 11.

Wheatstone Bridges are a particular type of resistive network made up of resistive elements. There are

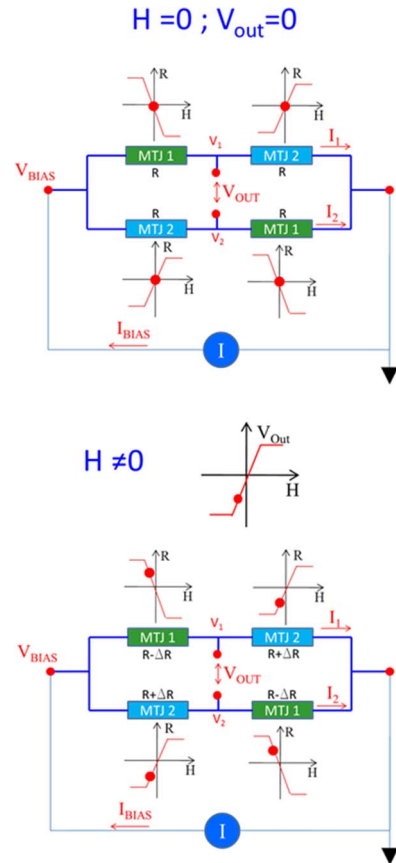


**Fig. 11.** (Top) A full Wheatstone Bridge made up of MR elements in the absence of an external magnetic field always has a null output voltage. (Bottom) An external magnetic field unbalances the bridge, causing a finite output voltage.

several topologies for the implementations of Wheatstone Bridges using MR elements, but from an application point of view, the most interesting is the Full Wheatstone Bridge, where all four resistive elements actively contribute for the output signal. To implement such a bridge, four identical MR sensors are required, but two must have a  $dR/dH$  that is symmetric with respect to the other two elements making up the bridge, as shown in Fig. 11.

The sensitivity of a Full Wheatstone Bridge made up of four identical MR elements is the same as an individual element. But unlike an individual MR sensor, if the resistance of the four MR elements is changed uniformly (as expected from temperature drifts), the contribution of such change to the bridge output is null. On the contrary, if a magnetic field is present, the four sensors of the bridge experience changes in resistance that are asymmetric. This unbalance causes a finite voltage at the bridge output terminals.

An issue in the manufacturing process of Full Wheatstone Bridges made of MR sensors concerns the method used to ensure that two of the bridge elements exhibit  $dR/dH > 0$ , while the remaining two exhibit  $dR/dH < 0$ . The simplest solution is of course to mechanically assemble identical elements along the same direction but in opposite senses, making all the required connections externally, via wire bonding or at a PCB level. This simple solution has three important drawbacks: 1) The mechanical assembly of individual components will always introduce alignment errors, which will limit the performance of the devices; 2) The mechanical assembly of individual elements is not cost-effective for the mass-production of magnetometers using such arrangement; and 3) Mechanical rotation cannot be used in compact applications requiring good spatial uniformity, since the individual elements will be too small to manipulate. When such constraints are present, a method to produce full Wheatstone Bridges at wafer level is required.

#### A. Wheatstone Bridge With GMR/Spin Valve Sensors

The production of Full Wheatstone Bridges with spin valve elements as MR sensors is relatively simple. To ensure that two of the elements have a  $dR/dH > 0$  while the two remaining ones have  $dR/dH < 0$ , the reference layer of the two sensor types must be directed along the same direction but in opposite senses.

A simple way of achieving such a goal is to deposit two stacks on the same wafer. The two stacks must be identical, and both must have a top-pinned reference layer. Top-pinned spin valves tend to have a well-defined exchange already deposited due to the fact that the fcc (111) texture of Cu will favor the fcc (111) texture of IrMn grown on top of it. As a result, the reference layer will be pinned without any further annealing

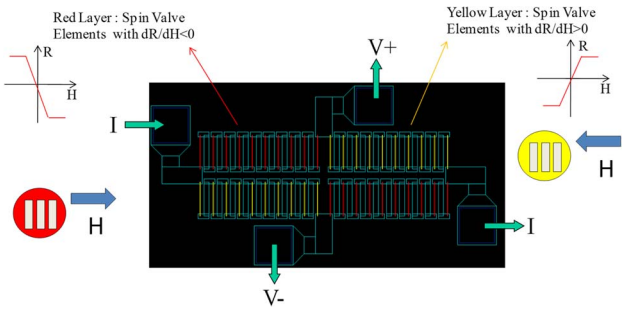


**Fig. 12. Example of a Full Wheatstone Bridge implemented with spin valve sensors. The spin valves drawn in red were deposited under a magnetic field along one sense, while the spin valves drawn in yellow were deposited under a magnetic field directed along the opposite sense, ensuring the opposite sign of  $dR/dH$ .**

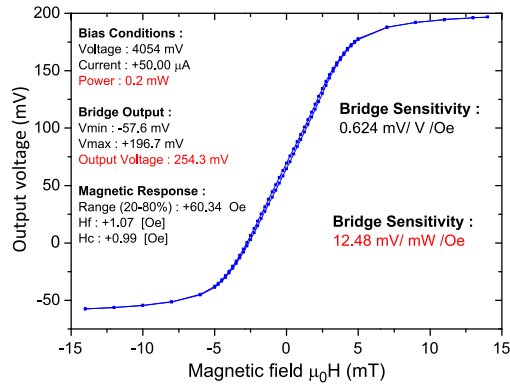
and the direction of the pinning field will be defined by the bias magnetic field used during the deposition. Therefore, to obtain the two classes of spin valves with opposite sign in  $dR/dH$ , all that must be done is to deposit the two stacks on different regions of the same wafer and rotate the direction of the bias magnetic field used during the deposition between the two deposition steps.

Fig. 12 shows a Full Wheatstone Bridge made using the method to deposit two stacks on different regions of the same wafer. The two classes of spin valves shown (red with  $dR/dH < 0$  and yellow with  $dR/dH > 0$ ) were deposited in the same wafer. The deposition region was delimited by lift-off, and once both stacks were deposited, all subsequent lithography steps were made simultaneously, ensuring that any lithographic errors are the same for both types of elements. Both spin valves types are made from the same stack: Glass/Ta 2/NiFe 3/CoFe 2/Cu 1.9/CoFe 2/Ru 8/CoFe 1.5/MnIr 6/Ta 10 [thicknesses in nm].

The bridge in Fig. 12 comprises four resistive elements, each made up of a series of 30 spin valves with individual dimensions of  $3 \times 170 \mu\text{m}^2$ . The aspect ratio of the individual spin valves ensures a linear response due to the strong demagnetizing field effect, and the serial connection of the 30 elements is used to increase the total resistance and thus to increase the output voltage of the bridge. The final bridge output is shown in Fig. 13. The geometry of Fig. 12 together with the spin valve stack, which exhibits a bulk MR of 8%, results in a bridge sensitivity of 0.624 mV/V/Oe.

#### B. Wheatstone Bridge With MTJ Sensors

This simple solution that provides good results when applied to spin valve MR sensors does not work with state-of-the art MTJ sensors based on CoFeB/MgO/CoFeB. In such MTJs, a post-deposition annealing is always required to crystallize the amorphous CoFeB and ensure the characteristic large TMR ratios of typically



**Fig. 13.** Output of the spin valve Full Wheatstone Bridge shown in Fig. 7.

200%. A side effect of this annealing is to define the pinning direction of the exchange field at the interface between the antiferromagnet and the reference SAF. Therefore, any asymmetry in the direction of the magnetic bias field used during deposition is reset during magnetic annealing. Two methods are used to selectively set reference layer direction in MTJ sensors.

The first method is based on a local annealing of the MTJ pillars upon patterning. For this method, a single MTJ stack is used to produce the two types of sensors in a Full Wheatstone Bridge. In this example, the stack used is the one shown in Fig. 14, with a CoFeB thickness of 1.45 nm. As shown in Fig. 14 and explained in section B, as the CoFeB layer becomes thinner, the effect of the MgO/CoFeB interfacial magnetic anisotropy becomes dominant, resulting in a linear transfer curve under an in-plane magnetic field.

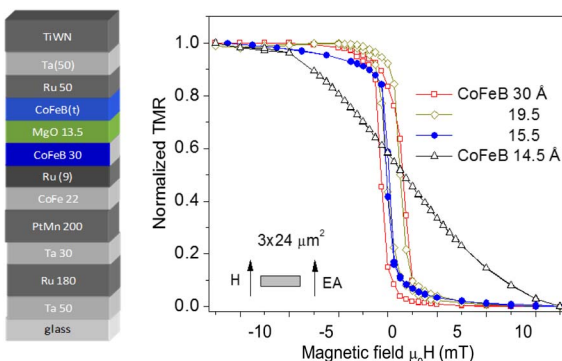


**Fig. 14.** MTJ stack used to produce an MTJ Full Wheatstone Bridge with a local annealing method. The stack made with a CoFeB thickness of 1.45 nm has a linear transfer curve under a field along the in-plane direction due to the dominant effect of the interfacial perpendicular magnetic anisotropy at the MgO/CoFeB interface.

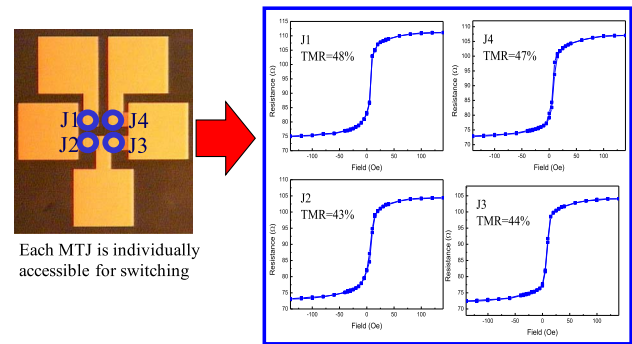


**Fig. 15.** (Left) Geometry used to pattern the four MTJ pillars in proximity and serially connected. (Right) Transfer curves of the individual MTJ pillars upon patterning and annealing. (Adapted from [31]).

This stack was patterned into MTJ pillars with areas of  $2 \times 6 \mu\text{m}^2$ , which exhibit a TMR of about 50%, a sensitivity of about 4%/Oe, and an  $\text{Rx}A \sim 1000 \Omega\mu\text{m}^2$ . The geometry chosen to pattern the pillars is shown in Fig. 15 [31].

Four pillars were connected in series with two electrical contacts connecting each of the pillars. With this geometry, any of the four pillars can be contacted individually, but they still don't make up a Wheatstone Bridge. Fig. 15 shows the individual transfer curves of a particular set of four pillars upon patterning and annealing at 320 °C for 30 minutes and cooldown under a 0.5 T field.

The next step required to make a Full Whetstone Bridge is to selectively rotate the direction of the pinning layer in two of the pillars. To this end, the substrate containing the MTJ sensors is heated up to a temperature close but below the blocking temperature of the PtMn pinning the SAF layer. Two of the pillars are then contacted with micropositioners, and a current is forced through them. The purpose of this current is to generate additional heat that is dissipated around the tunnel barrier, contributing to a local increase in temperature. Under the right conditions, the additional heat generated in the two pillars by the local current can raise the temperature of the PtMn above the blocking temperature. The exchange is lost while the current is flowing, and at this point, any external magnetic field applied during the cooling down of the substrate back to room temperature can be used to re-orient the reference layer. The conditions used for this selective local rotation of the pinned layer had to be optimized for the particular stack and geometry used in this example. It was found that the reversal could be achieved by homogeneously heating the substrate to a temperature of 240 °C and then applying a local current of 15 mA (current density of  $1.25 \times 10^5 \text{ A/cm}^2$ ) in the two pillars target for the reversal. The substrate was then cooled down under a field of 2000 Oe in the sense opposite to that used during the

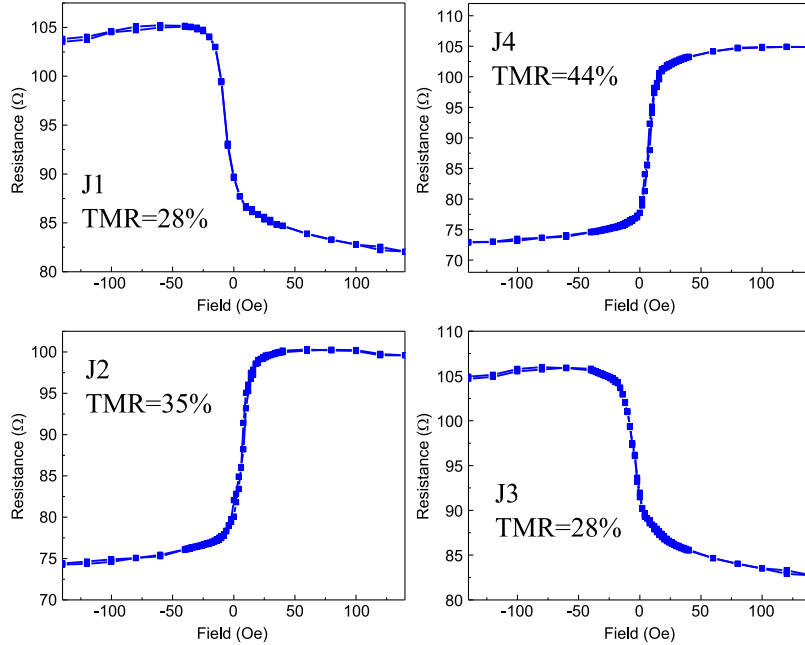


**Fig. 16.** Transfer curves of the individual MTJ pillars upon locally reversing the pinned layer direction of two pillars. Switching conditions require heating the substrate to a temperature of 240 °C and then applying a local current of 15 mA (current density of  $1.25 \times 10^5$  A/cm<sup>2</sup>) in the two pillars targeted for the reversal. The substrate was then cooled down under a field of 200 mT. (Adapted from [31]).

original annealing. Upon completion of this procedure, the transfer curves of the pillars shown in Fig. 15 were re-measured. The result is shown in Fig. 16.

Once the selective reversal of the pinned layer in two of the pillars is made, the Wheatstone Bridge can be made with a simple external connection, as shown in Fig. 17. The Wheatstone Bridge output is also shown on the right hand side.

This method is successful at producing a Full Wheatstone Bridge, and it is a nice demonstration of the ability

to locally reverse the reference layer in MTJ pillars. But it has several drawbacks. The most obvious ones are: 1) local heating is also not a good method for large-scale production; 2) there is an evident degradation of TMR in the reversed pillars that results in an unintended asymmetry between the bridge elements, which in turn degrades linearity and introduces offsets; and 3) this method is not independent of the MTJ RxA. In elements with a much larger RxA, the current necessary to reach the blocking temperature would require a voltage above the breakdown voltage of the dielectric barrier. Nevertheless, the method is successful, and the resulting Wheatstone Bridge in Fig. 17 exhibits a sensitivity of 14 mV/V/Oe, which is far more than the previous example based on spin valve sensors.

To overcome these limitations, a second method to selectively set the reference layer direction in MTJ sensors is introduced. To ensure compatibility with mass production, this method abandons the idea of any local interaction with the MTJ pillars as a mean to selectively set the reference layer. Therefore, the only way to have different orientations of the reference layer is to ensure that two stacks are present, which, under the same magnetic annealing conditions, end up with the reference layers at the interface with MgO directed along opposite senses.

One simple way of achieving this goal is shown in Fig. 18. The two stacks shown are identical in all regards, except that one stack incorporates a conventional

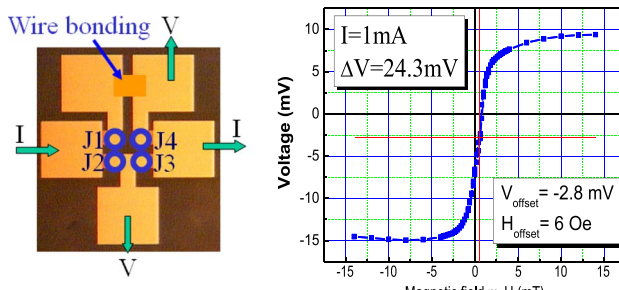


**Fig. 17.** (Left) Final wire-bonding connection that creates a Full Wheatstone Bridge out of the four pillars in Fig. 15. Upon establishing this connection, it is no longer possible to extract the transfer curves out of the individual pillars. (Right): Output of the resulting Full Wheatstone Bridge. (Adapted from [31]).

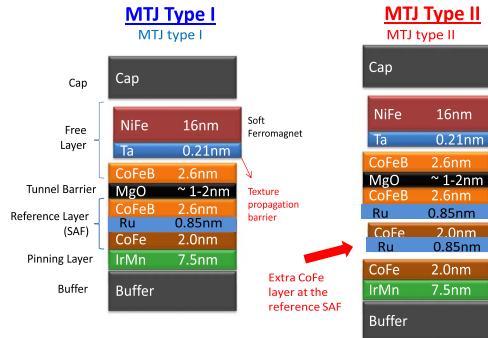


**Fig. 18.** Two MTJ stacks used to produce Wheatstone elements with opposite  $dR/dH$ , under the same annealing conditions.

SAF (type I: CoFe 2 nm/Ru 0.85 nm/CoFeB 2.6 nm), while the second one incorporates a three-layer unbalanced SAF (type II: CoFe 2 nm/Ru 0.85 nm/CoFe 2 nm/Ru 0.85 nm/CoFeB 2.6 nm). The extra layer introduced in the SAF has a single goal: under the same annealing conditions, the exchange field between the anti-ferromagnet and the first CoFe layer in both SAFs will be directed along the same direction. However, due to the uneven number of layers in the two stacks, the CoFeB at the interface with the MgO will be pointing toward opposite directions upon annealing.

The obvious drawback of this second method is the requirement of depositing two different stacks in the same wafer. This is not a simple task due to the extreme sensitivity of the MTJ Rx A to the MgO thickness. In particular, it is generally possible to deposit an MTJ in a substrate that has seen process steps since any etching results in additional substrate roughness, which might be enough to make the MgO barrier discontinuous. The

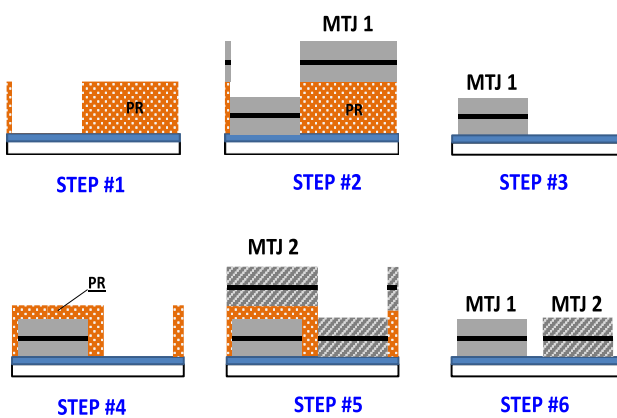


**Fig. 19.** Sequence of deposition and liftoff steps used to selectively define two different MTJ stacks in different areas of the same substrate wafer, using photoresist (PR) masks.

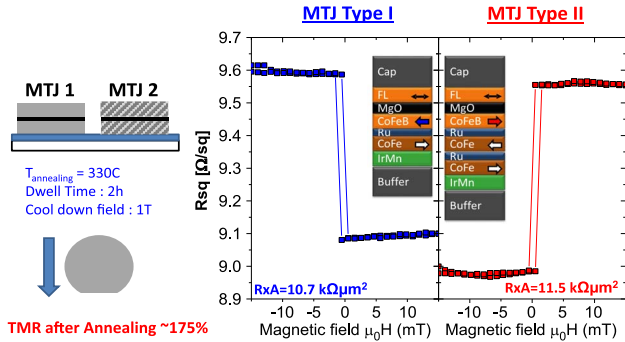


**Fig. 20.** TMR, Rx A, and bulk transfer curves obtained from the stacks of Fig. 13 deposited on the same wafer using lift-off delimited regions, as shown in Fig. 14.

best method to deposit the two stacks is to define two large areas with each of the two stacks in the same substrate by liftoff, as shown in Fig. 19. This will ensure that the surface where the second MTJ is deposited (in step 4 to step 5 of Fig. 19) has a roughness close to the original surface.

This is important because the two MTJ stacks must have similar figures of merit (TMR, Rx A, etc.) to avoid degradation of the Full Wheatstone Bridge response. The two stacks shown in Fig. 18 were deposited in a wafer and delimited, as shown in Fig. 19. To evaluate the stacks upon deposition, large test areas with about  $5 \times 5 \text{ mm}^2$  were defined. These areas are large enough to land CIPT probes, which were used to evaluate the TMR and the Rx A of the deposited stacks upon annealing at 330 °C for 2 h and cooling down under a magnetic field of 1 T. The results are shown in Fig. 20.

A TMR of about 175% is obtained for both stacks. The Rx A value is also similar but slightly asymmetric: an Rx A of 10.7 kΩμm<sup>2</sup> was obtained for an MTJ stack of Type I and an Rx A of 11.5 kΩμm<sup>2</sup> was obtained for an MTJ stack of Type II. This difference is within the error of margin of the method considering the set of tips used, the Rx A range, and the resistance of the lead in the two MTJs used. Besides the TMR and Rx A, the bulk transfer curves were also extracted from the CIPT measurement, confirming that the reference layer is pointing toward different directions in the two stacks, as shown in Fig. 20. This is a clear demonstration that the method just described is successful.

Upon defining these two MTJ stacks in the same wafer, MTJ pillars were patterned and connected in a full Wheatstone configuration, as shown in Fig. 21.

The large Rx A of the MTJ stacks used, the large bulk TMR of 175%, and with the large number of MTJ pillars connected in series contribute together to a very large

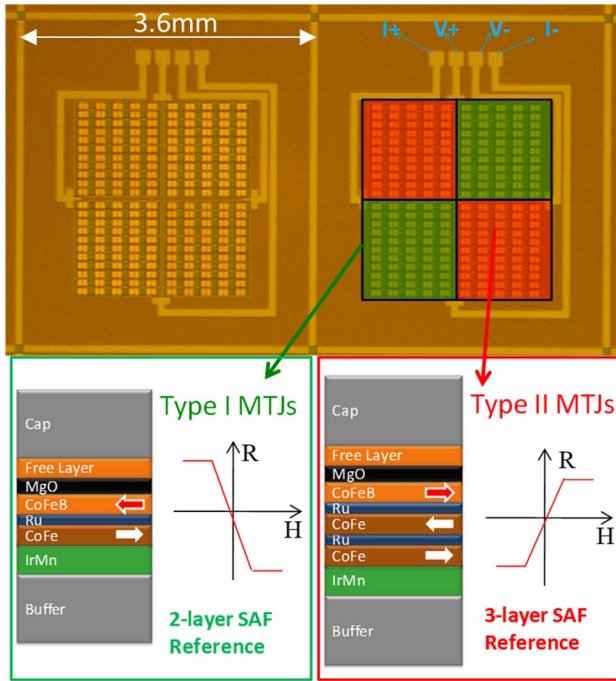


**Fig. 21.** Full Wheatstone Bridge made from the two MTJ stacks subjected to the same annealing conditions. Each resistive element making up the bridge comprises 110 MTJ pillars connected in series, with individual dimensions of  $5 \times 70 \mu\text{m}^2$ .

voltage output of the resulting bridge, even under the modest magnetic field. The output response of these MTJ Full Wheatstone Bridges is shown in Fig. 22 and is characterized by a sensitivity of 32.0 mV/V/Oe, which is the largest among the three examples described in this section.

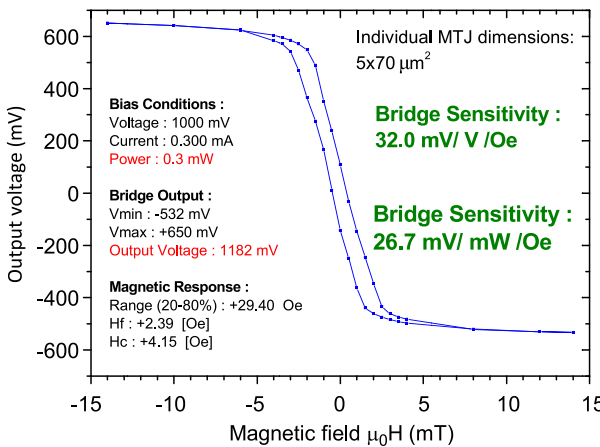


**Fig. 22.** Output of the MTJ Full Wheatstone Bridge obtained from two different stacks annealed under the same conditions.  
(Adapted from [64].)

Full Wheatstone Bridges are an important arrangement of MR sensors in several applications. The analysis of these solutions, which are used to produce bridges with MR elements, is described in Section IV-E, within the scope of a particular application: MR sensors for compass applications.

#### IV. MAGNETIC FIELD DETECTION LEVELS

Detecting small magnetic fields requires the optimization of the sensor output levels (signal) together with the noise control at the measuring frequency range. In general, there are several distinct contributions to the noise spectral density. In the particular case of MR devices, the noise sources that need to be considered are thermal noise, shot noise,  $1/f$  noise, and ferromagnetic resonance noise [32]. In MR sensors with a current-in-plane (CIP) configuration (spin valves and AMR), the  $1/f$  noise is given by

$$\left\langle \left( V_{\text{SV } 1/f}(f, t) \right)^2 \right\rangle = \gamma \frac{I^2 R^2}{N_C f} \Delta f \quad (2)$$

where  $N_C$  represents the number of carriers participating in the current  $I$  and  $\gamma$  is the phenomenological Hooge parameter (quantifies the intrinsic magnitude of the  $1/f$  noise for a specific device). In CPP geometry, the number of carriers is related to the device area and  $1/f$  noise is given by

$$\left\langle \left( V_{\text{MTJ } 1/f}(f, t) \right)^2 \right\rangle = \alpha_H \frac{I^2 R^2}{A f} \Delta f. \quad (3)$$

In this case, the parameter  $\alpha_H$  is the modified Hooge parameter. From (2) and (3), one can infer that the  $1/f$  noise spectral density at a specific frequency depends on the bias voltage ( $I^2 R^2 = V^2$ ), the device area, and the frequency considered. Comparing the  $1/f$  noise magnitude in different devices is therefore not straightforward, and the most unambiguous way to establish a comparison is through the magnitude of the Hooge parameter. Between two different devices, that which exhibits the lower value for the Hooge parameter will also have the lower  $1/f$  noise, with everything else being the same. A comparative discussion of the noise levels and detection limits for SV and TMR sensors can be found in [30]. Minimizing the value of the Hooge parameter is an important goal when producing sensors operating in the low frequency regime. Because charge trapping is one of the physical mechanisms originating  $1/f$  noise in TMR sensors, the barrier

thickness is an important parameter that influences the magnitude of  $1/f$  noise, thus increasing the tendency to reduce the RxA product with thinner barriers, as shown in Fig. 3(b).

### A. Incorporation of $N$ Magnetoresistive Elements

The use of arrays of MR sensors, connected in series and/or parallel, is a usual configuration in applications requesting high detectivities in detriment of high spatial resolution. The reasons will be explained next.

One of the usuals way to express the signal-to-noise in magnetoresistive sensors is to calculate the minimum detectable magnetic field for a given sensor over the frequency spectrum. To that end, the spectral noise density is expressed in units of magnetic field. For a sensor with a linear transfer curve characterized by a sensitivity  $dV/dH$  at a given field, the minimum detectable field is limited by the spectral noise density

$$S_H(f) \left[ \frac{T}{\sqrt{\text{Hz}}} \right] = \frac{S_V(f)}{\frac{dV}{\mu_0 dH}} \quad (4)$$

The two terms contributing in (4) have quite different behaviors when several magnetoresistive devices are connected in series. If  $N$  identical sensors characterized by an individual spectral noise density  $S_{1V}(f)$  are connected in series, the noise sources of the  $N$  sensors will not retain phase coherency among them. As a consequence, the spectral noise density of the series will scale proportionally to  $\sqrt{N}$

$$S_{NV}(f) = \sqrt{\sum_{n=1}^N S_{1V}^2(f)} = \sqrt{N} S_{1V}(f). \quad (5)$$

But that is not the case for  $dV/dH$ . If  $N$  identical sensors, each with a sensitivity of  $dV_1/dH$ , are added in series, the sensitivity of the full series will simply be proportional to  $N$

$$\frac{dV_N}{\mu_0 dH} = N \cdot \frac{dV_1}{\mu_0 dH}. \quad (6)$$

As a consequence, the field detection limit of a series of  $N$  identical sensors with an individual field detection limit  $S_{1H}(f)$  will decrease proportionally to  $\sqrt{N}$

$$S_{NH}(f) \left[ \frac{T}{\sqrt{\text{Hz}}} \right] = \frac{\sqrt{N} S_{1V}(f)}{\frac{NdV_1}{(\mu_0 dH)}} = \frac{1}{\sqrt{N}} S_{1H}(f). \quad (7)$$

Most sensing applications are made at low frequencies in a regime where  $1/f$  noise is by far the most important noise source, with thermal and shot noise being negligible. In such a limit, (7) can be expressed as

$$S_{NH}(f, H) \left[ \frac{T}{\sqrt{\text{Hz}}} \right] = \left( \frac{1}{R_N(H) \mu_0 dH} \right)^{-1} \sqrt{\frac{\alpha_H(H)}{N A_1} \frac{1}{f}}. \quad (8)$$

From (8), it is clear that to decrease the minimum field detection limit, the TMR must increase while the linear range must decrease, resulting in an overall increase of the sensitivity  $dR_N/dH$ . It is also clear that in this regime the resistance of the sensors will not affect the field detection limits. On the other hand, the field detection limit decreases with the square root of the total sensing area  $N A_1$ . Thus, at low frequencies when  $1/f$  noise is dominant, there is an important trade-off between spatial resolution and minimum field detection.

On the opposite end, for frequencies large enough for the  $1/f$  to be negligible, only white noise sources contribute to limit the magnitude of detectable fields. In such a regime, (7) takes the form

$$S_{NH}(f, H) \left[ \frac{T}{\sqrt{\text{Hz}}} \right] = \left( \frac{1}{R_N(H) dH} \right)^{-1} \sqrt{\frac{2e}{I_N} N \coth\left(\frac{q V_1}{2 K_B T}\right)}. \quad (9)$$

Here, for a given voltage  $V_1$  across each TMR sensor in a series of  $N$  elements, the minimum detectable field decreases with  $I_N$ , i.e., it decreases with the resistance of the MTJs in the series.

### B. Toward Pico-Tesla Detection at Room Temperature

Large series of 1102 MTJ sensors made of individual MTJ pillars with  $100 \times 100 \mu\text{m}^2$  was microfabricated [33]. A picture of this array, which covers an area of  $\sim 4 \times 6 \text{ mm}^2$ , is shown in Fig. 23. Notice that a (Ta/Cu) (low resistance) buffer was specially used to minimize interconnect resistance contribution, which is of major importance due to the large number of elements.

Here, the transfer curve of each element was linearized by soft-pinning the sensing layer in the direction orthogonal to the reference layer, as described in Fig. 5. The TMR stack used to this end was fine tuned to minimize the linear range ( $\pm 2 \text{ mT}$ ), thus maximizing  $dR/dH$  in (8) and (9). As a result, good linear response is obtained from the patterned device, as shown in Fig. 23(c).

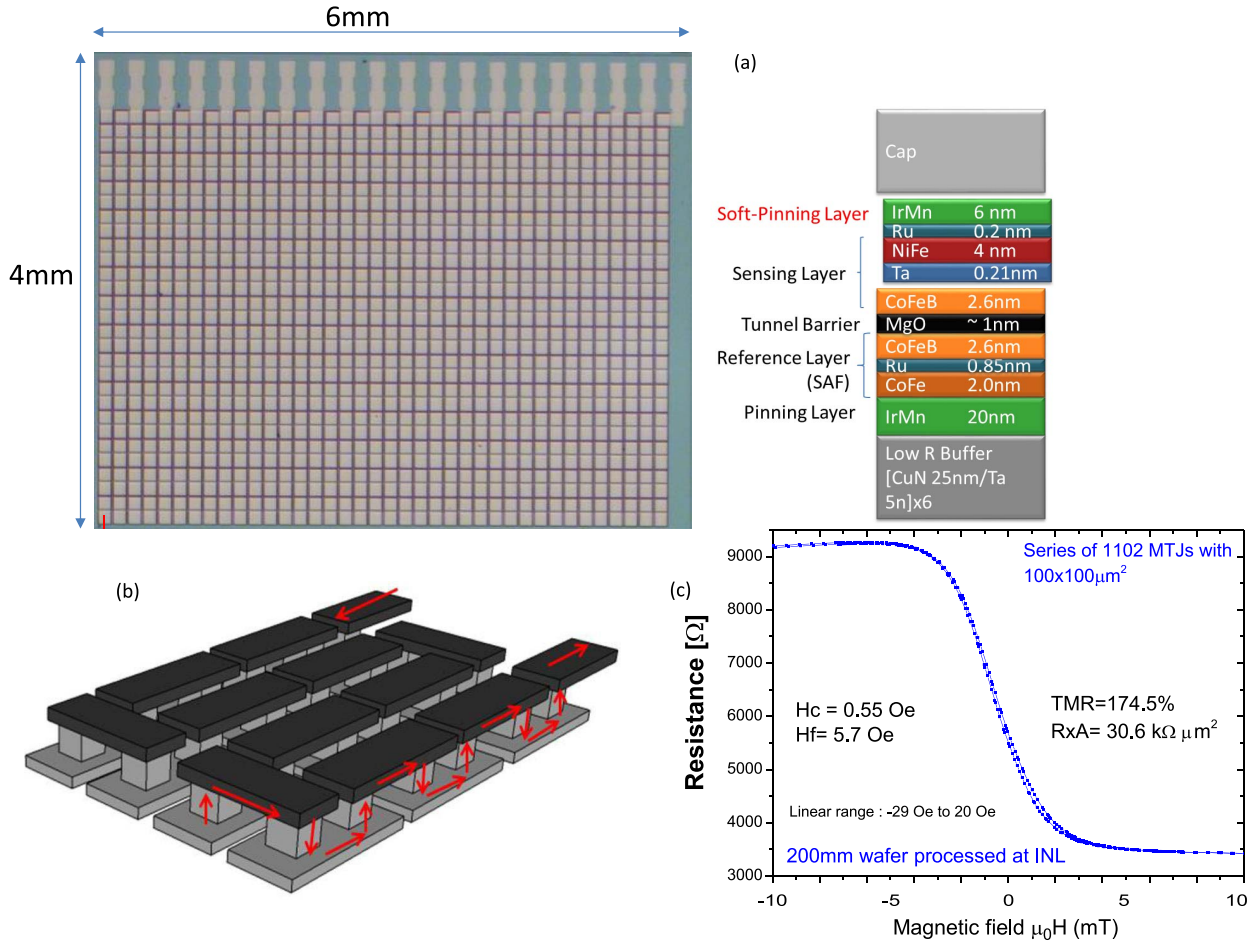


**Fig. 23.** (a) Optical image of an array of  $100 \times 100 \mu\text{m}^2$  MTJ sensors with 1102 sensors in series, (b) schematics of the MTJ element integration, and (c) device transfer curve. The stack structure is (thicknesses in nm): [5 Ta/25 CuNx6/5 Ta/5 Ru/20 IrMn/2 Co<sub>70</sub>Fe<sub>30</sub>/0.85 Ru/2.6 CoFe<sub>40</sub>B<sub>20</sub>/MgO/2 CoFe<sub>40</sub>B<sub>20</sub>/0.21 Ta/4 NiFe/0.20 Ru/6 IrMn/2 Ru/5 Ta/10 Ru. [Rx<sub>A</sub> is  $30.6 \text{ k}\Omega \cdot \mu\text{m}^2$ ].

The thickness of the MgO tunnel barrier was tuned to result in a resistance per individual device of about  $3 \Omega$ , which is the lowest possible value in the absence of non-uniform current distribution effects [34] within the  $100 \times 100 \mu\text{m}^2$  pillars with the leads used to contact the pillars.

In practical applications, the data from a sensor is always acquired by an ASIC or CMOS circuit. The overall sensitivity of the sensor is an important parameter to optimize, but the noise of the electronic circuit is equally important in the final performance. If the signal of the sensor is below the noise of the electronic data acquisition circuit, the minimum detectable field will always be out of reach of the integrated system. For this reason, the output of a sensor is usually amplified and conditioned before being digitized. This is one point in which the use of large TMR in series is highly advantageous with respect to more conventional solutions incorporating fully metallic MR sensors, such as Hall Sensors, AMR, or GMR. TMR sensors and TMR arrays in series have a much larger resistance. The downside of this fact is, of

course, a larger thermal noise background. But the upside is a larger output signal for the same magnetic field.

In this particular example, despite the very low resistance of each pillar ( $3\Omega$ ) that ensures a low thermal noise level, the full series with 1102 MTJs has a resistance of  $\sim 3 \text{ k}\Omega$  in the low resistance state and  $\sim 9 \text{ k}\Omega$  in the high resistance state. This means that  $dR/dH = 126.2 \text{ }\Omega/\text{Oe}$ . Such large sensitivities have very low requirements in terms of amplification and signal conditioning.

To illustrate this point, the series was characterized (details of the detection setup in [32]), with the purpose of determining the minimum detectable field in the absence of any amplification. Fig. 24 shows the results obtained by direct measurement of the magnetic field set by a coil in the region of the TMR array sensor.

## V. APPLICATIONS

In this section, we present some cases demonstrating the advantages of MR sensors. These examples were selected among the large spectra of reported applications.

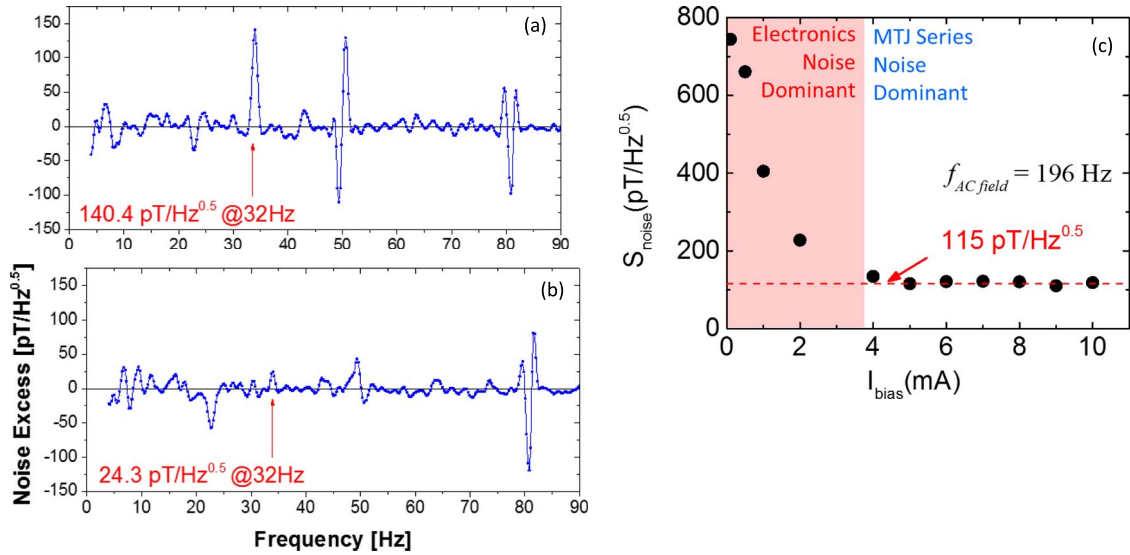


**Fig. 24.** Demonstration of the ability to detect a field of (a)  $140$  pT//Hz<sup>0.5</sup> and (b)  $24$  pT/Hz<sup>0.5</sup> at  $32$  Hz using a large array of MTJs after  $400$  averages. (c) Dependency of the minimum directly detectable field on the TMR sensor bias current.

### A. Application I: Probes for Biomedical Purposes

1) *Rigid Probes:* The full compatibility between the MR sensor technologies and the Silicon industry opened a realm of opportunities. One of them is related to the integration of MR sensors on sharp, machined tools for

biomedical applications. The ability to measure directly and locally, at room temperature, the magnetic fields related to human activity (e.g., brain, or heart) attracted increasing attention in past years [7]. *In vitro* experiments for brain activity monitoring upon electrical stimulation [Fig. 25(a)] require special sensor geometries,

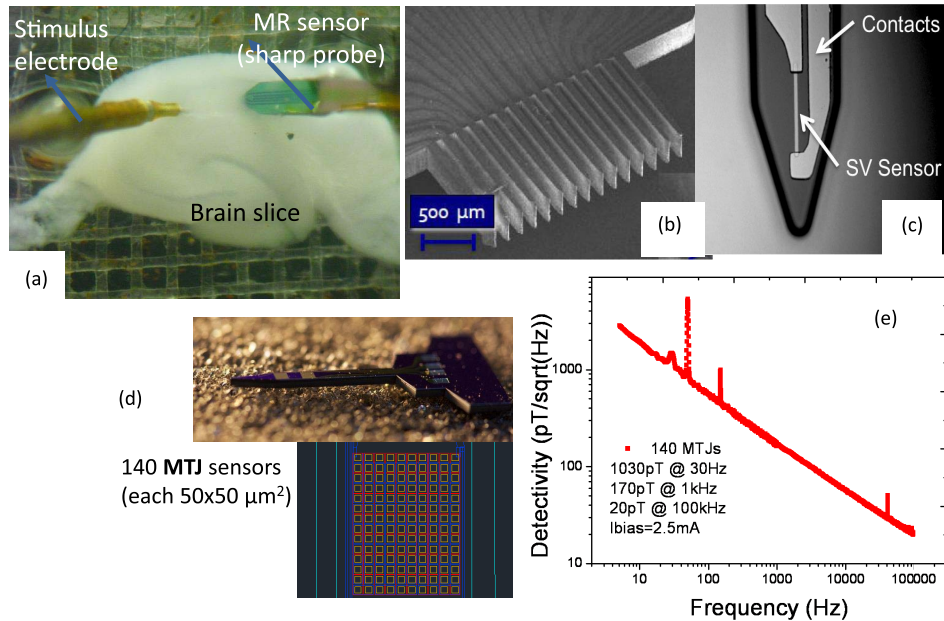


**Fig. 25.** (a) Monitoring postsynaptic activity *in vitro* by using an MR probe, (b) array of probes for multiplexing detection, (c) detail of the probe tip, with one sensor defined, (d) probe with  $140$  MTJ elements in series, for improved signal-to-noise-ratio, and (e) detectivity spectrum obtained from the noise spectrum, with a pronounced impact of the  $1/f$  noise, and minimum fields of  $170$  pT/Hz<sup>0.5</sup> at  $1$  kHz and  $20$  pT/Hz<sup>0.5</sup> at  $100$  kHz. [Credit: J. Valadeiro, INESC-Microsistemas e Nanotecnologias].

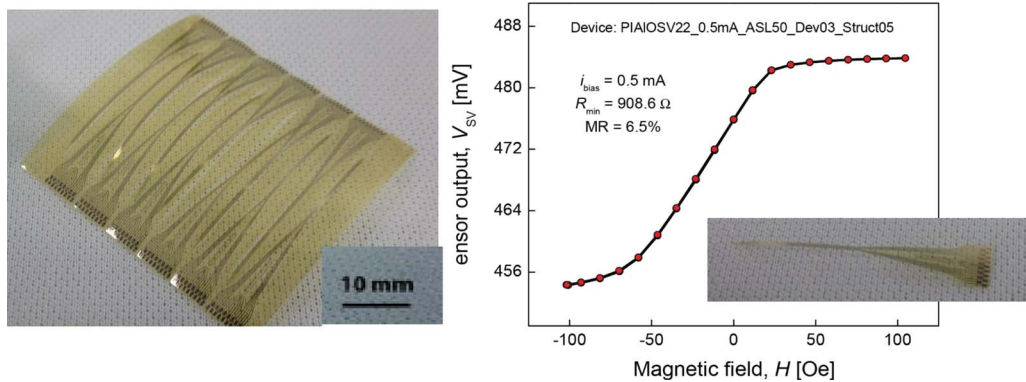


**Fig. 26.** (Left) Section of the microfabricated area, with several probes defined on 20  $\mu\text{m}$  thick polyimide substrate. (Right) Spin valve sensor transfer curve (measured after processing) after release. Inset shows the isolated probe. (Credit: J. Gaspar, Iberian Nanotechnology Laboratory, www.inl.int).

and sharp probes can incorporate single or large arrays of MR sensors [Fig. 25(b)–(d)], together with microelectrodes microfabricated under the same process line. The challenge is indeed the detection of very weak fields (fT to nT) that usually have a low frequency domain. Here, the 1/f noise is the dominant factor, as exemplified with the noise spectra of an MTJ array integrated in a sharp needle [Fig. 25(e)], estimating the minimum fields to be detectable by these sensors to be of the order of 20 pT at 100 kHz (far faster than the biological signals, below 30 Hz).

2) *Flexible Probes:* The progresses achieved recently in the integration of functional MR materials with flexible substrates (namely polyamide) inspired a realm of new devices and applications [37]. In parallel, MR technology has pushed the integration limits toward stretchable substrates [38], recently demonstrated. Although device performance is still degraded with the non-rigidity of the substrates [39], the impact on a flexible/bendable sensor solution is a strong driving motive for continued research, in particular for medical applications (inflatable balloon catheters, for example) microfabricated on flexible substrates that are able to bend and conform to the non-planar geometries.

The fabrication process based on polyimide (PI) benefit from their flexibility, thermal stability, chemical resistance, high mechanical modulus, and biocompatibility. One example that illustrates the successful integration of MR sensors (in this case a spin valve, but TMR sensors have also been measured on polyimide substrates [40]) is given in Fig. 26. Substrate thickness is 20  $\mu\text{m}$ , which requires microfabrication on a rigid substrate (Si), followed by deep Si etch and further material release [41]. The MR sensor maintains its magnetoresistance ratio when compared with rigid (Si or glass) substrates.

These probes are under evaluation for implantable devices, for which a large market has already been established for bendable electrodes (in neurosciences, for example). Incorporating magnetic field sensors in these tools would expand the limits of the MR technologies even further.

## B. Application II: MR Sensors for Nondestructive Testing

The detection of defects over large metal surfaces has impact on production and quality control on an industrial scale, and MR sensors can bring advantages over other technologies for eddy current detection [42] due to their very good spatial resolution. The use of coils to detect eddy currents in nondestructive testing (NDT) is limited to low frequencies; therefore, MR sensors are replacing them because they can operate over a large range of frequencies, namely on the inspection of ultrathin surface flaws (high-frequency application) and deep buried defects (low-frequency application). For these reasons, NDT based on MR technologies have been used as a tool to detect small surface cracks, evaluate metal medical implants [43], inspect printed circuit boards [44], detect corrosion, and inspect coin and bills [45], among others.

One possible architecture for NDT that is used to detect welding join defects in Aluminum alloy AA2024 plates is described here (see Fig. 27 [46]). For this application, the TMR sensor (array of 72 TMR elements, each with  $50 \times 50 \mu\text{m}^2$ , with a total active area of  $0.5 \times 0.5 \text{ mm}^2$  [see Fig. 27(c)]) is optimized to detect the vertical ( $z$ ) component of the magnetic field generated by induced eddy currents. These fields are of the order of a few Oe (0.1 mT) at the sensor position, and are very dependent on the material resistivity. MgO-based MTJs stack consists of  $[\text{Ta } 5/\text{CuN } 25]_{x6}/\text{Ta } 5/\text{Ru } 5/\text{IrMn } 20/\text{Co}_{70}\text{Fe}_{30} 2/\text{Ru } 0:85/\text{CoFe}_{40}\text{B}_{20} 2:6/\text{MgO } 1/\text{CoFe}_{40}\text{B}_{20} 2/\text{Ta } 0:21/\text{NiFe } 4/\text{Ru } 0:20/\text{IrMn } 6/\text{Ru } 2/\text{Ta } 5/\text{Ru } 10$

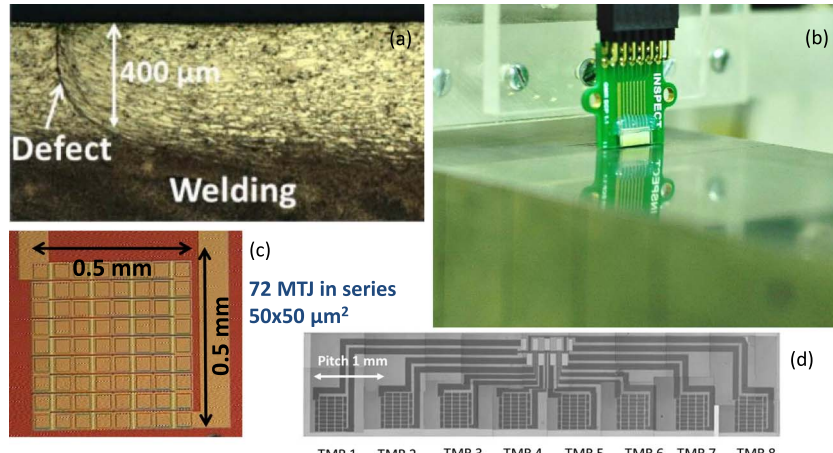


**Fig. 27.** Geometry used for NDT inspection of welding joints between two Al plates. (a) Cross section microscopy view of the joint section at the surface. (b) Setup used for the measurements, with the sensor chip mounted at the surface of the PCB, near an excitation line. (c) Microscope view of the TMR sensors (72 MTJ elements connected in series). (d) Global view of the eight sensors patterned on the chip. Developed in collaboration between INESC-MN and INESC-ID (Adapted from [50]).

(thicknesses in nm), with a resistance-area product of  $20 \text{ k}\Omega.\mu\text{m}^2$  [47], a linear range between  $-1$  to  $2.5 \text{ mT}$ , and sensitivity of  $94 \text{ V/T}$ . The sensor chip (comprising a line of 8 TMR sensors, with  $\sim 1 \text{ mm}$  pitch) is mounted on a PCB integrating an embedded current line (driver trace, width  $200 \mu\text{m}$ , thickness  $35 \mu\text{m}$ ) for field excitation over the Al plates, vertically separated by  $\sim 200 \mu\text{m}$  from the sensor surface.

The detection of the  $\sim 400 \mu\text{m}$  deep defect is done by setting the driver trace with an AC current of  $1 \text{ MHz}$  ( $f_1$ ) and measuring the magnetic field generated by the induced eddy currents with two MR sensors in differential mode ( $1 \text{ mm}$  pitch separation between sensors). Fig. 28 shows the schematics of the setup. Each TMR sensor was biased with a sinusoidal bias AC current of

$1.65 \text{ mA}_{\text{peak-to-peak}}$ , at  $999 \text{ kHz}$  ( $f_2$ ). The third generator creates a demodulation reference frequency at  $1 \text{ kHz}$ , the difference between  $f_1$  and  $f_2$ . This two-frequencies strategy modulates the magnetic information in frequencies  $f_1 - f_2$  and  $f_1 + f_2$ , whereas the combined contribution of the electric biasing and electromagnetic coupling appear at frequencies  $f_1$  and  $f_2$  respectively. The two sensors were connected in a differential configuration, and the produced signal was demodulated using a lock-in amplifier tuned at  $1 \text{ kHz}$  ( $f_1 - f_2$ ).

The TMR sensor is scanned over a large area of the Aluminum block to find the welding defect signature. The induced eddy currents are well distributed in space, and a defect translates in a discontinuity in the generated field, which is well detectable with these sensors, with a SNR of the order of  $38 \text{ dB}$ , as can be seen in Fig. 29.

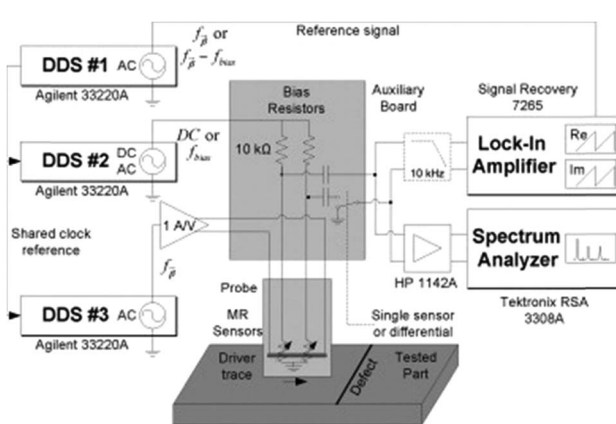


**Fig. 28.** Measurement setup for the NDT using MR sensors and excitation line [50]. Reprinted by permission from Elsevier (2014).

### C. Application III: MR Sensors for Power Measurement

Measuring both battery charge levels (in the power stations) and the battery state in the automotive field of electric vehicles is a key application where MR sensors have demonstrated performance. The direct measurement of power and current can also be associated with smart power meters within the energy distribution network (smart grid). Another possible product of MR technology is the design and construction of differential breakers and power-consumption-limiting devices.

We describe here the design of a Wheatstone Bridge current sensor using TMR elements. Each of the four resistances of the bridge consists of 360 TMR single elements connected in series for improved electrical robustness and improved signal-to-noise levels (Fig. 30). The TMR stack was (thickness in nm): Ta 5/CuN 50/Ta

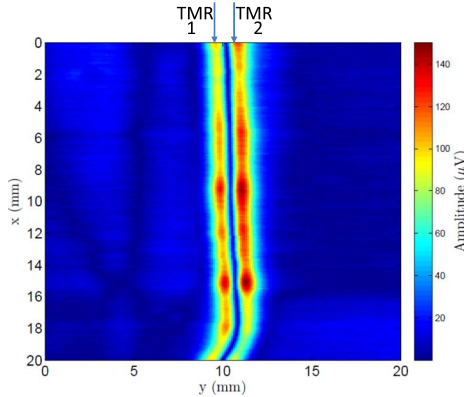


**Fig. 29.** Result of the scanning measurement, carried out with two TMR sensors separated by a pitch of 1 mm. The defect region is unequivocally localized out of the scanned area of the Al block.

3/CuN 50/Ta 3/Ru 5/MnIr 6/CoFe2/Ru 0.85/CoFeB 2.6/MgO 1/CoFeB 3/Ta 0.21/NiFe 16/Ta 10/CuN 30/Ru 7. Material resistance-area is  $R_A = 100 \Omega \cdot \mu\text{m}^2$ , and each TMR element has the dimensions of  $2 \times 30 \mu\text{m}^2$ . Device characterization for single MTJ elements and for elements connected in series is described in [48] and [49]. While near 160% of tunnel magnetoresistance is measured in a single TMR element, increased contact resistance due to processing issues lead to a reduction to 120% in its corresponding series elements connection. The transfer curves have a small hysteresis effect and a sensitivity of  $7.33 \Omega/\text{Oe}$  in a 75 Oe linear range.

A PCB was designed to incorporate a U-shaped copper trace (1.1 mm separation distance between sensor and trace). The surrounding space was occupied by ambient

air, keeping a proper thermal impedance to avoid excessive sensor heating originated in the trace.

In this case, a full Wheatstone Bridge is accomplished even for all TMR elements mounted in the same orientation (single chip, no reversal of the reference layer): each element of the bridge ( $R_1, R_2, \dots$ ) are located in specific places on the chip, where the magnetic field created by the U-shape current line have opposite directions. Using a Wheatstone Bridge configuration removes the contribution of parasitic magnetic fields and improves the thermal stability.

This application is one good example in which the large area occupied by the series MTJ ( $\sim 1 \times 0.3 \text{ mm}^2$ ) is not an obstacle, and the advantages of series configurations (described in Section IV) are highlighted.

The sensor DC sensitivity was characterized in Fig. 31, showing the sensor output voltage dependency on an external DC current sweeps of  $\pm 10 \text{ A}$ ,  $\pm 20 \text{ A}$ , and  $\pm 30 \text{ A}$  current amplitudes applied to the copper trace. From these experimental measurements, an average of  $9.8 \text{ mV/A}$  sensitivity was obtained for the bridge-MTJ current sensor. This value is at least one order of magnitude higher than the sensitivity showed by spin-valve-based current sensors [50], [51].

This application has been assessed as a smart wattmeters network that provides information about the power delivered to a load [52]. The proposed system is a clear example of applicability of MR sensing in daily industrial and domestic environments. It will provide users of electrical energy with immediate access via a smart mobile device to the consumption cost of an industrial machine or appliance derived from its daily use. The information provided becomes key when choosing more energy-efficient equipment.

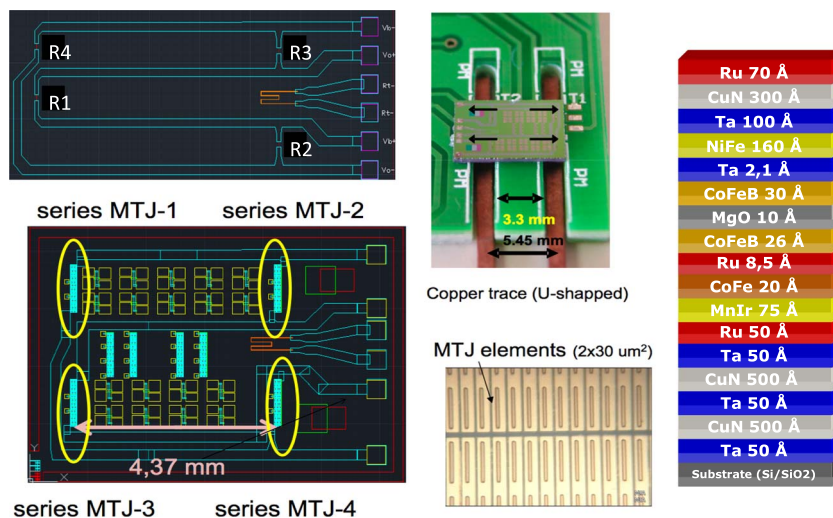


**Fig. 30.** Geometry and mask layout used for power and current measurement. Four TMR sensors (each consisting of 360 elements connected in series) are mounted in Wheatstone Bridge, over a power line (Adapted from [51]).

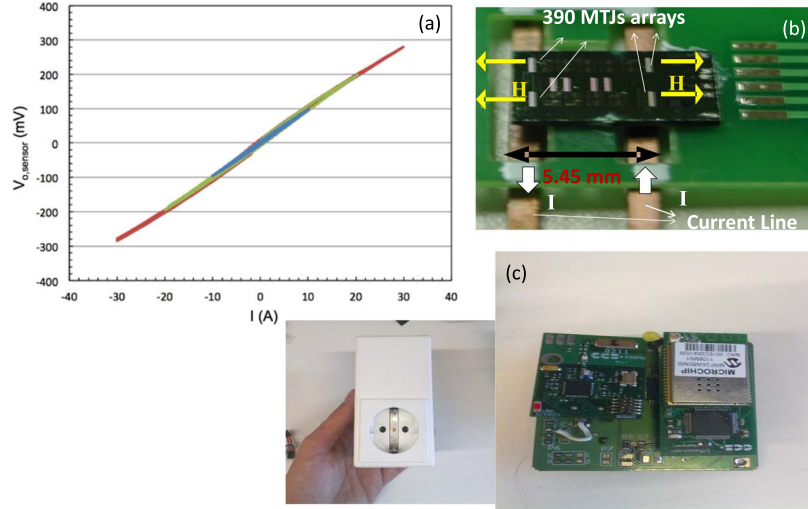


**Fig. 31.** (a) Full Wheatstone Bridge voltage output dependency on the power line current. Device sensitivity is 9.8 mV/A. (b) Chip integration on the PCB, with the magnetic field direction indicated over each TMR sensor. (c) Final device developed jointly between University of Valencia, Spain and INESC-MN (Adapted from [49]).

#### D. Application IV: MR Sensors for Lab-on-Chip

MR sensors have been integrated for biological applications, such as biochips. The concept, described in detail in [53] and [54], relies on the sensor capability to detect the fringe field generated by magnetized nano/microparticles attached to biomolecules. Fig. 32 illustrates the concept with 250 nm superparamagnetic beads. Notice that manipulation of these particles and biomolecules requires handling fluidic samples, so additional passivation layers (typically a combination of \$\text{Si}\_3\text{N}\_4\$ and \$\text{Al}\_2\text{O}\_3\$ films, up to 500 nm thick in total) are needed to prevent electrolyze through the metal leads during experiments. Moreover, the labeling particles

should be handled under minimum aggregation, preferably in a paramagnetic state. Only upon setting a local magnetic field near the sensor the particles will reveal some magnetic moment so to generate the detectable fringe field.

As a representative example, the biochip developed at INESC-MN [55] and shown in Fig. 33 integrates spin valve sensors (\$2.5 \times 80 \mu\text{m}^2\$, U-shaped). Furthermore, a current line surrounding the sensor was specially designed to enable particles focusing onto the sensing area [56]. For biochip applications, an Au pad is patterned on top of the spin valve (above the passivation layer, setting a sensor-to-surface separation of

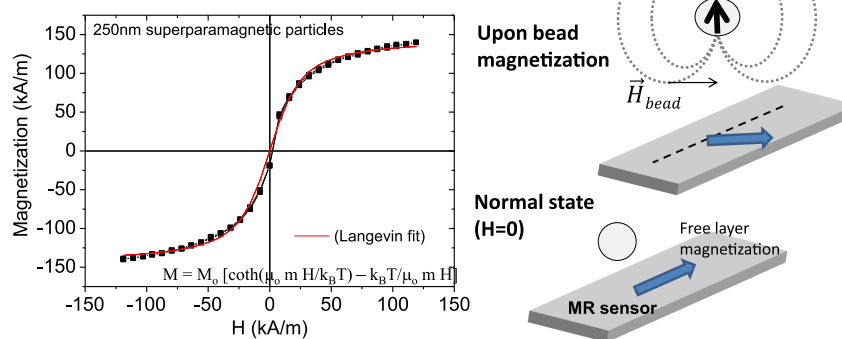


**Fig. 32.** Magnetic characteristic ( $M$  vs.  $H$ ) of the nanoparticles used for biochips. At the normal state (where no field is applied), the particles have no effect on the MR sensor. When a field is applied to magnetize the particles, they create a fringe field capable of rotating the free layer, thus changing the MR sensor resistance.

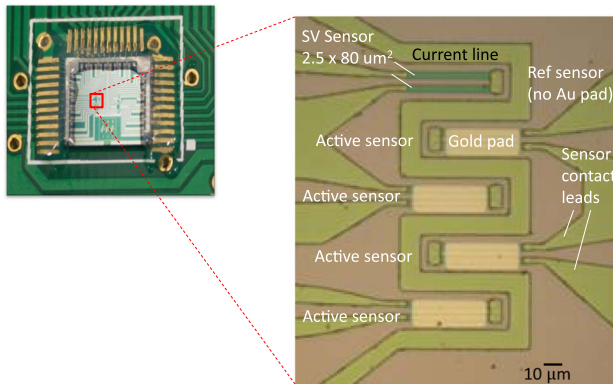


**Fig. 33.** Biochip layout, including four groups of five U-shaped spin valves surrounded by a U-shaped current line. The sensor is covered by a  $13 \times 43 \mu\text{m}^2$  Au pad for biological functionalization. The sensor stack is deposited by an ion beam deposition in a Nordiko 3000 tool, with the typical structure Si/500 Å Al<sub>2</sub>O<sub>3</sub>/20 Å Ta/30 Å Ni<sub>80</sub>Fe<sub>20</sub>/25 Å Co<sub>81</sub>Fe<sub>19</sub>/26 Å Cu/25 Å Co<sub>81</sub>Fe<sub>19</sub>/60 Å Mn<sub>76</sub>Ir<sub>24</sub>/30 Å Ta/150 Å Ti<sub>10</sub>W<sub>90</sub> (N).

400 nm) to define the area in which the biological probes are immobilized.

The MR sensor chip is mounted into a PCB to a portable measurement set-up that provides all the electronic circuitry to address and read out the sensors (Fig. 34). To reduce the noise and the thermal drift of the sensors, the detection of the magnetic particles is made using a DC + AC external, in a plane, magnetic field. The AC field is used to magnetize the particles (as described in Fig. 32). The sensor output signal is amplified, digitally filtered, and sent via USB to a laptop.

The control of sample loading and washing steps was achieved using a microfluidic channel (U-shape, PDMS channel, 300-μm width, 100-μm height, to assure assay reproducibility.

Measurements carried out on the detection of *Salmonella* cells are presented in Fig. 35. Binding was detected through a change of the sensor output voltage, and after cleaning the chip surface, the sensor with the Au pad functionalized for *Salmonella* produced a remaining signal of 210 μV. These results confirm that the magnetic labelled cells were able to be recognized by the immobilized molecules and remained attached even after intensive washing.

The research on MR biochips has inspired a new generation of entrepreneurs, with multidisciplinary skills, covering electronics, materials, physics, biology, and medicine. The combination of these MR biochips to electronic [57] and microfluidic platforms allow sample manipulation, temperature control, multiplexing signal acquisition and processing, converting a bulky and complex analytical apparatus into a lab-on-a-chip device. Some start-up companies that emerged from the research panorama are as follows. 1) MagArray [58] originated from Stanford University in 2005, aiming to develop and commercialize a diagnostic platform dedicated to clinical tests for cardiac biomarker and research in cancer diagnostics assays. The demonstrators incorporate SV and TMR sensors integrated with CMOS. 2) Zepto Life Technology [59] originated from the University of Minnesota in 2004, aiming to deliver portable devices for early detection of cancer, based on GMR multilayer technology. 3) Magnomics [60] originated in 2014 from research institutes INESC-MN and INESC-ID, and using MR technology for molecular diagnostics, aiming to identify the pathogenic bacteria in milk for animal health applications. As an emerging field (still at present), magnetic biosensors have highly benefited from the maturity of MR sensors not only in the performance (large-scale production, reliability, and costs) but also on the versatility that MR technology offers while integrating with most of the technologies supporting lab-on-a-chip devices.

In particular, multiplexing electronics through integrated CMOS-ASICs [61], and microfluidics (PDMS or glass) need to be highlighted. Irreversible surface binding between SiO<sub>2</sub> or Si<sub>3</sub>N<sub>4</sub> is possible through irradiation with Oxygen plasma, at low voltages, and compatible with MR technologies. This method has been used for applications using high fluidic pressure (cytometer, separation modules), which is not suitable for microchannel clamping methods. However, chip reuse after biological assays requires additional cleaning protocols, and finally the ensemble chip + microchannel becomes disposable. For this reason, the cost of MR chips needs to be as low as possible, which imposes serious limitations for the integrated electronics

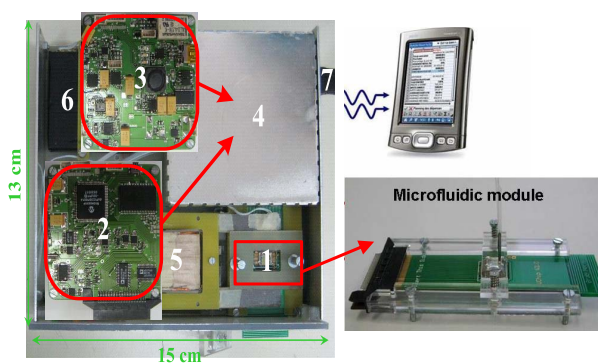


**Fig. 34.** Prototype of a portable electronic platform for biochip readout. Developed through a collaboration between INESC-MN and INESC-ID [57]. (1) PCB incorporating also the microfluidic channel. (2) Sensing and processing module. (3) Communication module and magnetic drive circuits. (4) Noise shielding. (5) Coil for the magnetic drive. (6) Battery. (7) USB connector.

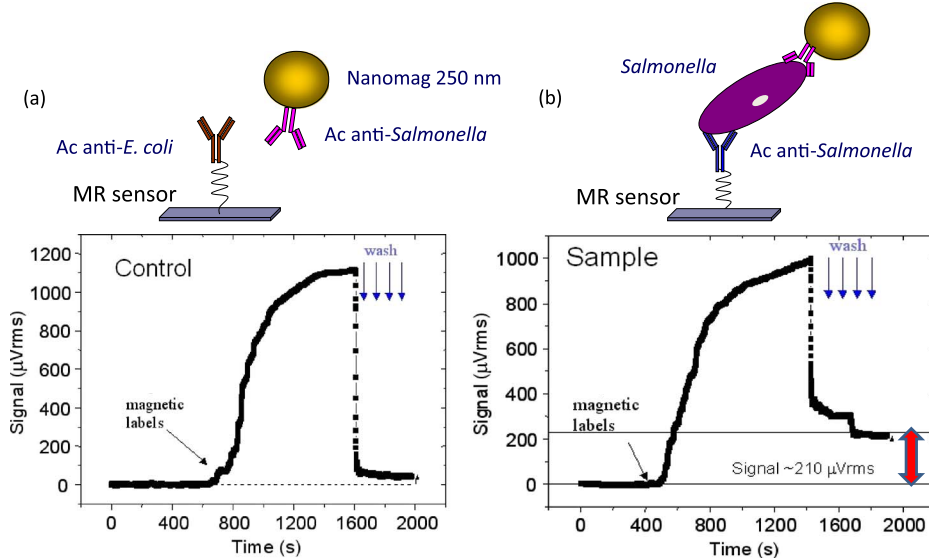


**Fig. 35. Schematics of the immobilization method and real time sensor response during detection of antibody-antigen recognition event. (a) No linking occurs; therefore, upon washing, the background signal approaches the initial value (b) with the correct surface chemistry over the sample sensor (immobilized anti-Salmonella antibodies and magnetically-labeled Salmonella cells covering the Au pad), and the remaining signal allows quantification of the Salmonella concentration over the chip.**

(ASIC-CMOS). For MR biochips, the detection is static, thus a top pressuring system can bring enough sealing during the experiments. One monolithic architecture integrating U-shape spin valve sensors [63] is presented in Fig. 36. The MR sensor is patterned on a CMOS chip module, and the ensemble further bonded onto a microfluidic channel. The noise of each matrix element is further characterized and compared to the noise of a standalone spin valve, and a portable electronic platform is designed to perform biological assays. Although the noise is still higher, the spin valve integrated on the CMOS chip enables an increase in density and compactness of the measuring electronics. The success of this solution is being assessed by Magnomics.

#### E. Application V: MR Sensors for Compass Applications

Magnetometers are a common component in many industrial applications. A good example of such applications are those related to the automotive industry.

A modern day car incorporates nearly 100 different magnetic field sensors, which are mostly used to detect the relative position of rotating parts, such as the steering wheel, the throttle pedal, or the windshield wipers. Most of these magnetometers are still implemented using Hall sensors, but the share of GMR-based magnetometers is increasing, and the entry of MTJ bases sensors in this market is in its infancy. To illustrate the advantages/disadvantages of different types of MR sensors, three different magnetometers were evaluated for a very specific application: the detection of geomagnetic

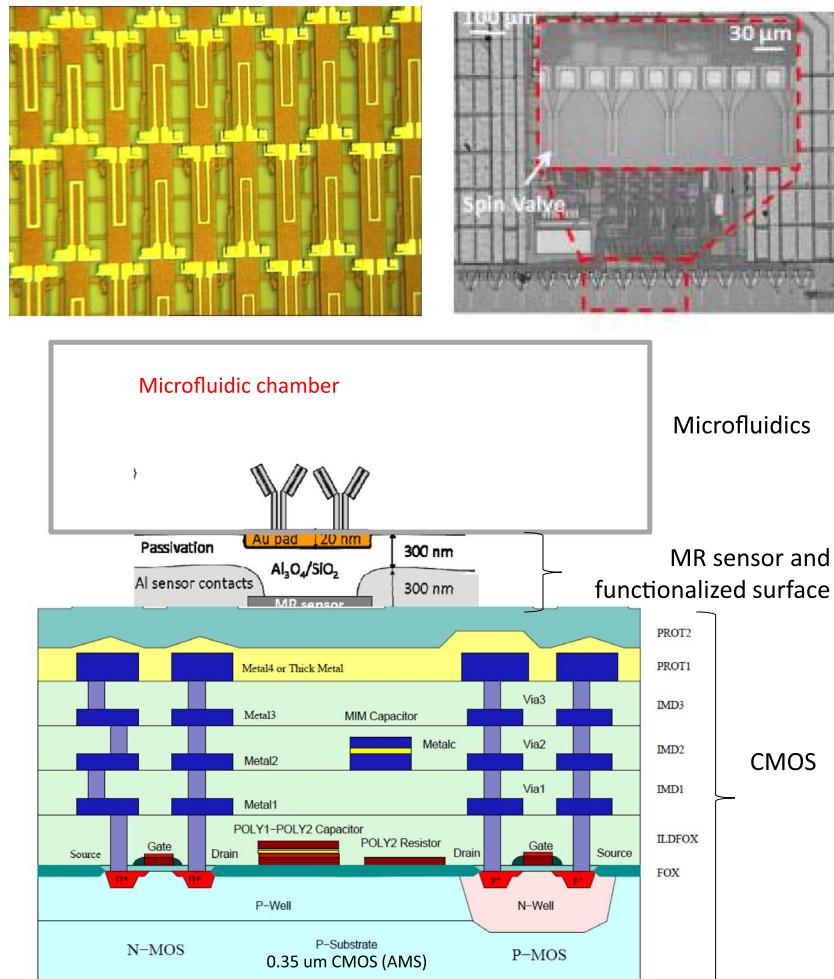
fields. The end-goal of this effort concerned the production of a GPS unit capable of tracking the vehicle position, in the event of a sudden loss of GPS signal, such as those experienced when entering tunnels of crossing bridges, until the GPS signal is recovered. A key ingredient for such improved GPS tracking is a digital compass, which in turn obtains the beating from the readout of an analog magnetometer. The prototype system, which includes the analog magnetometer described next, is shown in Fig. 37.

A key requirement for such an application is that the sensor readout should not depend on the temperature. Whether it is spring or winter, the sensor should provide consistent readings. For this reason, the magnetometers tested in this application were manufactured in Wheatstone Bridge configuration [64], as described in Section III.

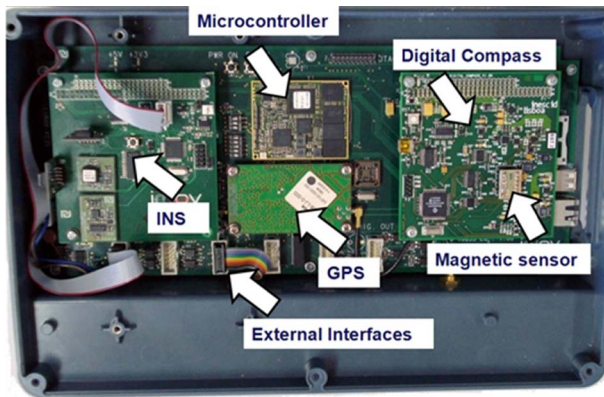
Three different solutions were compared as resistive elements of a Full Wheatstone Bridge: single MTJ pillars (with the reference layer set with a local current assisted annealing), spin valve series (two stacks, no annealing, reference direction set during deposition), and MTJ series (with two stacks and reference direction set during annealing).

Table 2 summarizes the main figures of merit established for each solution.

The approach that uses a single MTJ solution is the one operating at a lower voltage. This is a limitation imposed by the dielectric breakdown of the tunnel barrier. Above 0.6 V, the bias voltage becomes too close to the breakdown voltage, endangering the durability of the



**Fig. 36.** (Top) Integration of MR sensors (256 U-shape SV elements) on a CMOS chip, with the requiring electronic addressing of multiple sensors, making use of a complex network of wiring, amplifiers, and multiplexers. Developed through the collaboration between INESC-MN and INESC-ID [55]. (Bottom) Cross view of the complete CMOS + Sensor + microfluidic architecture.



**Fig. 37.** Improved GPS prototype incorporating a digital compass unit. This prototype was produced by INESC-ID, INESC-INOV and INESC-MN within the European project SE2A: Security and Energy Efficiency for Automotive.

solution. The pressure to increase the bias voltage as much as possible is related to the voltage output. The larger the bias voltage, the higher the output for a given external field. Compared with series of spin valves the voltage output for a 1 Oe (0.1 mT) output is larger in the single MTJ, but at the expense of a much higher power consumption: 4 mW versus 0.2 mW. Furthermore, the bias dependence of the TMR becomes apparent. The voltage output of the single MTJ solution decreases sharply from 13.6 mV/V/Oe at 90 mV bias voltage down to 6.08 mV/V/Oe with a bias voltage of 600 mV. The solution based on a series of MTJs is clearly the best solution out of the three examples in Table 2 and Section III. The MTJ series has a very large sensitivity (32 mV/V/Oe) and low power consumption (26.6 mV output per mW of bias power per Oe). The TMR bias dependence is unnoticed up to a bias voltage of 4 V, which ensures an output of 128 mV under a 1 Oe (0.1 mT) field. This output is larger than that obtained

**Table 2** Key Figures of Merit for Three Wheatstone Bridge Magnetometers Using Different MR Technologies [Source: INESC-MN]

	Single MTJ	Spin Valve Series	MTJ Series
Sensitivity	13.6 mV/V/Oe [V=90mV] 6.8 mV/V/Oe [V=600mV] <b>1.02 mV/mW/Oe</b> [V=600mV]	<b>0.624 mV/V/Oe</b> 12.48 mV/mW/Oe	<b>32.0 mV/V/Oe</b> <b>26.7 mV/mW/Oe</b>
Bias Voltage	0.6 V <b>(Limited by intrinsic MTJ properties)</b>	4 V <b>(Limited by measurement setup : can withstand up to 80V)</b>	4 V <b>(Limited by measurement setup : can withstand up to 80V)</b>
Bias Current	6.667mA	0.050mA	1.200mA
Bias Power	4 mW	0.2 mW	4.8mW
Voltage change sweeping 1 Oe field	4.08 mV	2.496 mV <b>(Limited by the setup bias voltage limit)</b>	128 mV <b>(Limited by setup bias voltage limit)</b>

with a single MTJ and with a series of spin valves by a factor of 32 and 51, respectively. This is an important factor since a larger output power for a given field reduces the requirements for digitizing electronics with an improvement in SNR, cost, and footprint.

Note that the sensitivities stated in Table 2 is the average sensitivity across the full linear range. As shown in Fig. 38, for the case of the MTJ series, the linearization was not fully effective. This is attributed to the linearization strategy chosen (based on the demagnetizing field) and slightly large MTJ dimensions ( $5 \times 70 \mu\text{m}^2$ ). As result, the reversal is not completely smooth, with several domains visible in the transfer curve, and the coercivity is considerably large (4.15 Oe–0.415 mT). Still, a small loop transfer curve is linear and free of hysteresis (as shown in the inset of Fig. 38). But some domains

are still visible, and the local sensitivity around zero field is reduced with respect to the average value, from 32.0 mV/V/Oe down to 13.3 mV/V/Oe.

In the final application, two magnetometers based on the MTJ series Full Wheatstone Bridges were mechanically assembled at a relative orientation of 90°. The set of the two bridges was used as a 2-D magnetometer, with one sensor detecting the field magnitude along the XX direction and the second one detecting the field magnitude along the YY direction, as shown in Fig. 38. The

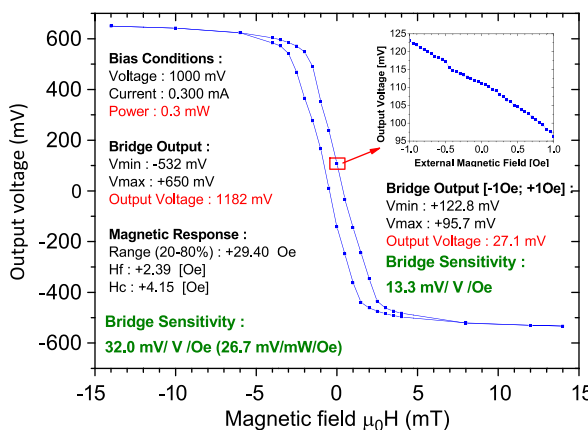


**Fig. 38.** MTJ series sensitivity at two different ranges. The inset shows the small loop response of the MTJ series under an external field between 1 Oe and +1 Oe. While the output of the sensor is free of hysteresis, several domains are visible due to imperfect linearization of the sensor, which also result in a reduced sensitivity around 0 field (Adapted from [64]).

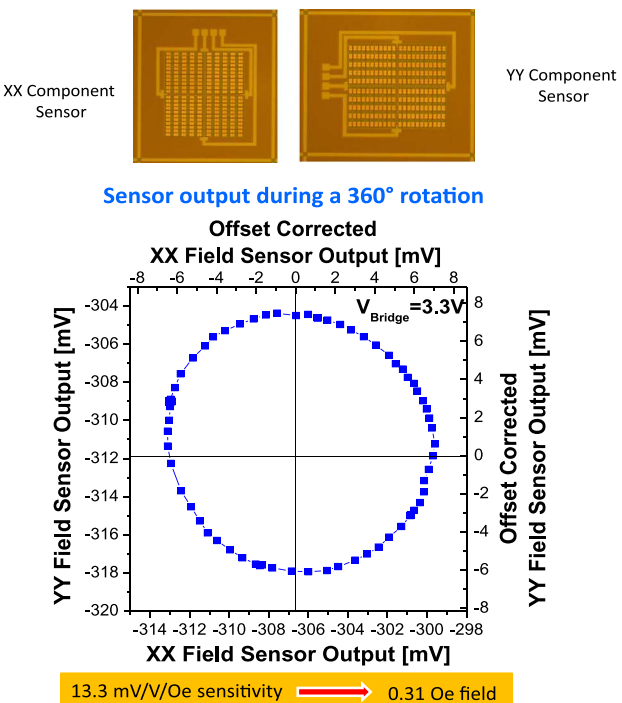


**Fig. 39.** 2-D magnetometer output under a 360° rotation subjected to no other excitation besides the geomagnetic field. No amplification was used. (Adapted from [64]).

output of the two sensors was logged under a bias voltage of 3.3 V, slightly below that of Table 2 and plotted in Fig. 39. The imperfect circle in the graphics is attributed to the mechanical errors setting the orientation of the two magnetometers in a 90° angle. Still, an output

between 6 mV and + 6 mV is obtained for each axis without any kind of amplification. This is a very large output, which is consistent with a magnetic field magnitude of about 0.31 Oe, considering the local sensitivity of the magnetometer around a null field. ■

## REFERENCES

- [1] J. Allred, R. Lyman, T. Kornack, and M. Romalis, "A high-sensitivity atomic magnetometer unaffected by spin-exchange relaxation," *Phys. Rev. Lett.*, vol. 89, 2002, Art. no. 130801.
- [2] S. Bandyopadhyay and M. Cahay, "Proposal for a spintronic femto-Tesla magnetic field sensor," *Physica E*, vol. 27, pp. 98–103, 2005.
- [3] J. Zhai, Z. Xing, S. Dong, J. Li, and D. Viehland, "Detection of pico-Tesla magnetic fields using magneto-electric sensors at room temperature," *Appl. Phys. Lett.*, vol. 88, pp. 062510-1–062510-3, 2006.
- [4] H. A. M. van den Berg, W. Clemens, G. Gières, G. Rupp, W. Schelter, and M. Vieth, "GMR sensor scheme with artificial antiferromagnetic subsystem," *IEEE Trans. Magn.*, vol. 32, p. 4624, 1996.
- [5] K. LePhan, H. Boeve, F. Vanhelmont, T. Ikkink, F. de Jong, and H. de Wilde, "Tunnel magnetoresistive current sensors for IC testing," *Sensors Actuators A*, vol. 129, pp. 69–74, 2006.
- [6] S. X. Wang et al., "Towards a magnetic microarray for sensitive diagnostics," *J. Mag. Magn. Mat.*, vol. 293, pp. 731–736, 2005.
- [7] J. Amaral et al., "Integration of MgO-based sensors in Silicon needles for magnetic measurements of neurons," *IEEE Trans. Magn.*, vol. 49, no. 7, pp. 3512–3515, 2013.
- [8] R. I. Potter, "Magnetoresistance anisotropy in ferromagnetic NiCu alloys," *Phys. Rev. B*, vol. 10, p. 4626, 1974.
- [9] M. N. Baibich et al., "Giant magnetoresistance of (001)Fe/(001)Cr magnetic superlattices," *Phys. Rev. Lett.*, vol. 61, p. 2472, 1988.
- [10] B. Dieny et al., "Spin-valve effect in soft ferromagnetic sandwiches," *J. Magn. Magn. Mater.*, vol. 93, p. 101, 1991.
- [11] M. Lederman, "Performance of metallic antiferromagnets for use in spin-valve read sensors," *IEEE Trans. Magn.*, vol. 35, pp. 794–799, 1999.
- [12] H. A. M. van den Berg, W. Clemens, G. Gières, G. Rupp, W. Schelter, and M. Vieth, "GMR sensor scheme with artificial antiferromagnetic subsystem," *IEEE Trans. Magn.*, vol. 32, p. 4624, 1996.
- [13] G. J. Simmons, "Generalized formula for the electric tunnel effect between similar electrodes separated by a thin insulating film," *J. Appl. Phys.*, vol. 34, p. 1793, 1963.
- [14] M. Jullière, "Tunneling between ferromagnetic films," *Phys. Lett.*, vol. 54A, p. 225, 1975.
- [15] D. Wang, C. Nordman, J. M. Daughton, Z. Qian, and J. Fink, "70% TMR at room temperature for SDT sandwich junctions with CoFeB as free and reference layers," *IEEE Trans. Magn.*, vol. 40, p. 2269, 2004.
- [16] S. Ikeda et al., "Tunnel magnetoresistance of 604% at 300 K by suppression of Ta diffusion in CoFeB/MgO/CoFeB pseudo-spin-valves annealed at high temperature," *Appl. Phys. Lett.*, vol. 93, 2008, Art. no. 082508.
- [17] X. F. Han, S. S. Ali, and S. H. Liang, "MgO(001) barrier based magnetic tunnel junctions and their device applications," *Sci China-Phys Mech Astron.*, vol. 56, p. 2960, 2013.
- [18] S. Cardoso, V. Gehanno, R. Ferreira, and P. P. Freitas, "Ion Beam deposition and oxidation of spin dependent tunnel junctions," *IEEE Trans. Magn.*, vol. 35, pp. 2952–2954, 1999.
- [19] P. P. Freitas, R. Ferreira, S. Cardoso, and F. Cardoso, "Magnetoresistive sensors," *J. Phys.: Condens. Matter*, vol. 19, 2007, Art. no. 165221.
- [20] A. Silva, D. Leitao, J. Amaral, J. Valadeiro, S. Cardoso, and P. P. Freitas, "Linearization strategies for high sensitivity magnetoresistive sensors," *Eur. Phys. J. Appl. Phys.*, vol. 72, 2015, Art. no. 10601.
- [21] B. Dieny, "Spin Valves," in *Magnetoelectronics*, M. Johnson, Ed. New York, NY, USA: Elsevier, 2004, ch. 2.
- [22] K. Klaassen, X. Xing, and J. van Peppen, "Signal and noise aspects of magnetic tunnel junction sensors for data storage," *IEEE Trans. Magn.*, vol. 40, pp. 195–202, 2004.
- [23] R. Janeiro et al., "Linearization and field detectivity in magnetic tunnel junction sensors connected in series incorporating 16nm-thick NiFe free layers," *IEEE Trans. Magn.*, vol. 48, no. 11, pp. 4111–4114, 2012.
- [24] B. Negulescu et al., "Wide range and tunable linear magnetic tunnel junction sensor using two exchange pinned electrodes," *Appl. Phys. Lett.*, vol. 95, no. 11, 2009, Art. no. 112502.
- [25] J. Y. Chen, J. F. Feng, and J. M. D. Coey, "Tunable linear magnetoresistance in MgO magnetic tunnel junction sensors using two pinned CoFeB electrodes," *Appl. Phys. Lett.*, vol. 100, no. 14, 2012, Art. no. 142407.
- [26] R. Ferreira, E. Paz, P. Freitas, J. Wang, and S. Xue, "Large area and low aspect ratio linear magnetic tunnel junctions with a soft-pinned sensing layer," *IEEE Trans. Magn.*, vol. 48, pp. 3719–3722, 2012.
- [27] S. Ikeda et al., "A perpendicular-anisotropy CoFeB-MgO magnetic tunnel junction," *Nature Materials*, vol. 9, p. 721, 2010.
- [28] P. Wisnioski, J. M. Almeida, S. Cardoso, N. P. Barradas, and P. P. Freitas, "Effect of free layer thickness and shape anisotropy on the transfer curves of MgO magnetic tunnel junctions," *J. Appl. Phys.*, vol. 103, no. 7, p. 07A910, 2008.
- [29] J. M. Teixeira et al., "Exchange biased CoFeB-MgO tunnel junctions at the onset of perpendicular anisotropy with in-plane/out-of-plane sensing capabilities," *J. Appl. Phys.*, vol. 111, no. 5, 2012, Art. no. 053930.
- [30] P. P. Freitas et al., "Optimization and integration of magnetoresistive sensors," *SPIN*, vol. 1, no. 1, pp. 71–91, 2011.
- [31] J. Cao and P. P. Freitas, "Wheatstone bridge sensor composed of linear MgO magnetic tunnel junctions," *J. Appl. Phys.*, vol. 107, no. 9, p. 09E712, 2010.
- [32] E. R. Nowak, M. B. Weissman, and S. S. P. Parkin, "Electrical noise in hysteretic ferromagnet-insulator-ferromagnet tunnel junctions," *Appl. Phys. Lett.*, vol. 74, p. 600, 1999.
- [33] E. Paz, S. Serrano-Guisan, R. Ferreira, and P. P. Freitas, "Room temperature direct detection of low frequency magnetic fields in the 100 pT/Hz<sup>0.5</sup> range using large arrays of magnetic tunnel junctions," *Appl. Phys.*, vol. 115, 2014, Art. no. 17E501.
- [34] J. Chen, Y. Li, J. Nowak, and J. Fernandez de-Castro, "Analytical method for two dimensional current crowding effect in magnetic tunnel junctions," *J. Appl. Phys.*, vol. 91, p. 8783, 2002.
- [35] V. Gehanno et al., "Ion beam deposition of Mn-Ir spin valves," *IEEE Trans. Magn.*, vol. 35, p. 4361, 1999.
- [36] P. P. Freitas, S. Cardoso, R. Sousa, W. Ku, and R. Ferreira, "Spin dependent tunnel junctions for memory and read head applications," *IEEE Trans. Magn.*, vol. 36, no. 5, pp. 2796–2801, 2000.
- [37] M. Melzer, G. Lin, and O. G. Schmidt, "Stretchable spin valves on elastomer membranes by predetermined periodic fracture and random wrinkling," *Adv. Mater.*, vol. 24, no. 48, pp. 6468–6472, 2012, doi: 10.1002/adma.201201898.
- [38] C. Barraud et al., "Magnetoresistance in magnetic tunnel junctions grown on flexible organic substrates," *Appl. Phys. Lett.*, vol. 96, 2010, Art. no. 072502.
- [39] M. Melzer et al., "Stretchable magnetoelectronics," *Nano Lett.*, vol. 11, pp. 2522–2526, 2011.
- [40] J. Gaspar et al., "Fabrication and mechanical characterization of flexible devices with sensors with magnetoresistance responses above 150%," presented at the INTERMAG Conference, Beijing, China, 2015.
- [41] International Iberian Nanotechnology Laboratory. [Online]. Available: [www.inl.int](http://www.inl.int)
- [42] E. E. Kriezis, T. D. Tsiboukis, S. M. Panas, and J. A. Tegopoulos, "Eddy currents: Theory and applications," *Proc. IEEE*, vol. 80, no. 10, pp. 1559–1589, 1992.
- [43] T. Dogaru and S. T. Smith, "Giant magnetoresistance-based eddy-current sensor," *IEEE Trans. Magn.*, vol. 37, p. 3831, 2001.
- [44] Y. Dalichaouch, A. L. Singsass, F. Putris, A. R. Perry, and P. V. Ciprott, "Low frequency electromagnetic technique for nondestructive evaluation," in *Proc. SPIE*, 2000, vol. 3994, pp. 2–9.
- [45] Wuxi Lertech Co., Ltd., <http://lertech.com>
- [46] L. Rosado, F. Cardoso, S. Cardoso, P. Ramos, P. Freitas, and M. Piedade, "Eddy currents testing probe with magneto-resistive sensors and differential measurement," *Sensors and Actuators A: Physical*, vol. 212, pp. 58–67, 2014.
- [47] F. Cardoso et al., "Magnetic tunnel junction based Eddy current testing probe for detection of surface defects," *J. Appl. Phys.*, vol. 115, no. 17, pp. 17E516-1–17E516-3, May 2014.
- [48] D. Ramírez Muñoz, J. Sánchez Moreno, S. Casans Berga, and A. E. Navarro Antón, "Active power analog front-end based on

- a Wheatstone-type magnetoresistive sensor," *Sensors Actuators A*, vol. 169, pp. 83–88, 2011.
- [49] J. Sánchez *et al.*, "Magnetic tunnel junction current sensor for industrial applications," *IEEE Trans. Magn.*, vol. 48, no. 11, pp. 2823–2824, 2012.
- [50] M. Tondra, J. M. Daughton, D. Wang, R. S. Beech, A. Fink, and J. A. Taylor, "Picotesla field sensor design using spin-dependent tunneling devices," *J. Appl. Phys.*, vol. 83, p. 6688, 1998.
- [51] J. Sánchez, D. Ramírez, S. Cardoso, S. Casans, A. E. Navarro, and P. P. Freitas, "A non-invasive thermal drift compensation technique applied to a spin-valve magnetoresistive current sensor," *Sensors*, vol. 11, pp. 2447–2458, 2011.
- [52] D. Ramírez, J. Sanchez, S. Cardoso, and P. P. Freitas, "Dispositivo y sistema de medida analógica de potencia eléctrica por magnetoresistencia," Spanish patent #P201331141, 2013.
- [53] P. P. Freitas *et al.*, "Spintronic platforms for biomedical applications," *Lab-on-Chip*, vol. 12, no. 3, pp. 546–557, 2012.
- [54] G. Li, S. X. Wang, and S. Shouheng, "Model and experiment of detecting multiple magnetic nanoparticles as biomolecular labels by spin valve sensors," *IEEE Trans. Magn.*, vol. 40, pp. 3000–3002, 2004.
- [55] V. C. Martins *et al.*, "Femtomolar Limit of Detection with a Magnetoresistive Biochip," *Biosensors Bioelectronics*, vol. 24, no. 8, pp. 2690–2695, 2009.
- [56] H. A. Ferreira *et al.*, "Rapid DNA hybridization based on AC field focusing of magnetically labeled target DNA," *Appl. Phys. Lett.*, vol. 87, p. 013901, 2005.
- [57] J. Germano *et al.*, "A portable and autonomous magnetic detection platform for biosensing," *Sensors*, vol. 9, no. 6, pp. 4119–4137, 2009.
- [58] MagArray, Inc. [Online]. Available: <http://www.magarray.com>
- [59] Zepto Life Technology, LLC. [Online]. Available: <http://www.zeptolife.com/>
- [60] MAGNOMICS | Nanotech for Life Sciences. [Online]. Available: <http://www.magnomics.pt/>
- [61] D. Hall *et al.*, "A 256 Pixel Magnetoresistive Biosensor Microarray in 0.18  $\mu\text{m}$  CMOS," *IEEE J. Solid-State Circuits*, vol. 48, pp. 1290–1301, 2013.
- [62] B. H. Jo, L. M. van Lerberghe, K. M. Motsegood, and D. J. Beebe, "Three-dimensional microchannel fabrication in polymethylsiloxane (PDMS) elastomer," *J. Microelectromech. Syst.*, vol. 9, pp. 76–81, 2000.
- [63] F. A. Cardoso *et al.*, "Integration of magnetoresistive biochips on a CMOS circuit," *IEEE Trans. Magn.*, vol. 48, no. 11, pp. 3784–3787, 2012.
- [64] R. Ferreira, E. Paz, and P. P. Freitas, "2-axis magnetometers based on full wheatstone bridges incorporating magnetic tunnel junctions connected in series," *IEEE Trans. Magn.*, vol. 48, no. 11, pp. 4107–4110, 2012.

## ABOUT THE AUTHORS

**Paulo P. Freitas** received the Ph.D in solid state physics from Carnegie Mellon University, Pittsburgh, PA, USA, in 1986, followed by a Postdoctoral stay at IBM Watson Research Labs, Yorktown Heights, NY, USA.



He has been a Full Professor with the Physics Department of Instituto Superior Técnico, Lisbon, Portugal, the Leader of the Magnetics and Spintronics group, and Director of INESC Microsistemas e Nanotecnologias. Since 2009, he joined the International Iberian Nanotechnology Laboratory (INL-Braga), where he is a Deputy Director. He received several awards and distinctions related to his work on magnetoresistive biochips and bioelectronics, magnetoresistive sensors, MRAMs, and read heads for ultra high density recording. He is the author of more than 400 scientific articles, holds three patents, and is the inventor of a bioelectronic device. Prof. Freitas supervised 17 Ph.D. students, more than 20 postdoctoral fellows, and develops an intense educational mission to train and coach new scientists and engineers.

**Ricardo Ferreira** received the Ph.D. in physics engineering from Instituto Superior Técnico (IST) in 2008 upon his work on ion beam deposited magnetic tunnel junctions targeting hard disk drive read heads, nonvolatile memories, and magnetic field sensor applications.



He is a Researcher with the International Iberian Nanotechnology Laboratory (INL), where he is the Principal Investigator of the Spintronics Research group and the Coordinator of the ICT research area. INESC Microsistemas e Nanotecnologias was the host

institution during his Ph.D. and also the lab where he conducted his research as a Post-Doctoral Fellow until joining INL. At INL, the work has been focused on the production of MTJs using MgO barriers and the development of two high-yield and high-uniformity fabrication processes on 200 mm wafers. The current research goals include production of pT magnetic field sensors, the production of devices that explore the spin transfer effect (STT nano-oscillators, MRAM cells), the incorporation of perpendicular magnetization materials on MTJs, and the integration of MTJs with MEMS and CMOS devices. He is the co-author of 65 peer-reviewed publications.

**Susana Cardoso** received the Ph.D. in physics engineering from Instituto Superior Técnico (IST), Lisbon, Portugal, in 2002.



Since 2002, she has been a Senior Researcher at INESC Microsistemas e Nanotecnologias (MN) and the co-Leader of the Magnetics and Spintronics group. She is also an Associate Professor with the Physics Department, IST, Lisbon. She is the co-author of over 240 publications (researcher ID: B-6199-2013). She has coordinated several national projects and participated in several EU projects. She is responsible for student training and of services provided by INESC-MN to external partners. Her research interests include advanced thin films in large area wafers, microsystems, and optimization of magnetoresistive sensors for challenging applications.